IJME

Int. J. of Applied Mechanics and Engineering, ???, vol.???, No.???, pp.???-???
DOI: 10.59441/ijame/224469

MATHEMATICAL INVESTIGATION ON MHD BLOOD FLOW THROUGH A STENOSED ARTERY UNDER VARIABLE VISCOSITY AND BODY ACCELERATION

S. Kumar[1, 2*] and S. Kumar[3]
[1]Department of Mathematics, Government College for Women, Gurawara, Rewari, Haryana, INDIA
[2]University Institute of Engineering and Technology, Maharshi Dayanand University, Haryana, INDIA
[3]Department of Mathematics, University Institute of Engineering and Technology,
Maharshi Dayanand University, Haryana, INDIA
E-mail: sumit96105@gmail.com

This study investigated the effect of cylindrical-shaped hybrid nanoparticles on the flow of magnetohydrodynamic blood through a narrowed artery, considering the impact of body acceleration and the variable viscosity of blood, which is temperature-dependent. The mathematical flow equations have been converted into a dimensionless form, and the solution is obtained using the finite difference scheme. Graphs are used to illustrate the influence of controlling flow parameters on various physical properties such as velocity, concentration, temperature, heat transfer coefficient, mass transfer coefficient, flow rate, and wall shear stress. It is observed that the velocity profiles exhibit a pronounced enhancement with increasing values of the parameters solutal Grashof number, Prandtl number, and body acceleration parameter, indicating their direct role in accelerating the flow dynamics. In contrast, the parameters magnetic field and Reynolds number exert a suppressing influence, leading to a noticeable reduction in velocity profile. Furthermore, the temperature profiles rise with increasing concentration of copper nanoparticles, alumina oxide nanoparticles, and hybrid nanoparticles, due to the significant enhancement in effective thermal conductivity. This improved heat transport capacity facilitates greater energy absorption and elevates the overall temperature profile of the blood. Finally, the WSS increases with a rise in the thermal Grashof number, as buoyancy-driven forces strengthen blood motion near the arterial wall. In contrast, an increase in the magnetic field parameter suppresses blood velocity through Lorentz force resistance, thereby reducing wall shear stress. The findings could be valuable insights into blood flow behavior in the stenosed artery, applied therapeutically within the biomedical sciences.

Keywords: viscosity, nanoparticles, body acceleration, stenosed artery, hybrid nanoparticles.

1. Introduction

The mortality rate due to cardiovascular diseases (CVD) in both men and women in the world has significantly risen. The primary reason for this is the accumulation of plaque and atherosclerosis within the artery, which causes the flow diameter of the artery to become more constricted. As a result, a sufficient amount of blood is unable to reach the organs and tissues. The most popular and reliable method of diagnosis for cardiovascular disease (CVD) among medical professionals is angiography. As part of this therapy procedure, a catheter with a small diameter is introduced into the artery. This allows for the removal of cholesterol and lipids from the interior of the artery [1-4].

Nanofluids consist of tiny particles usually ranging from *1* to *100* nanometres, suspended in a base liquid. Choi and Eastman [5] detailed the characteristics of nanofluids in a study they released in 1995. The researchers found out that the addition of nanoparticle suspension to the underlying liquid caused an increase in temperature of the mixture, and hence the idea of applying the use of nanofluids as the heat transfer fluid. The gold nanoparticles are a way through which medicines are transported and released because of their unique physical and chemical properties [6-10]. Nanotechnology and its application in various disciplines

[*] To whom correspondence should be addressed

have interested researchers in various disciplines, such as thermal engineering, healthcare, as well as industry, in the past few decades. The tiny particles are known as nanoparticles and enhance the thermal characteristics of the fluid [6, 11]. Several types of nanomagnetic particles, such as microspheres and nanoparticles used as tracers or imaging agents when applied in blood flow measurements. The fact that these particles are not affected by the magnetic field allows placing them into the bloodstream in a controlled way. Flow patterns are visualized and analyzed, the dynamics of the vascular system studied, and drug delivery in the blood monitored without any problems. These substances are inert in nature and this ensures that they will have minimal effects on the physiological nature of blood not to mention that they provide valuable information to the goals of medical research.

Under the curved artery, Poonam and Sharma [12] used the Crank-Nicolson method to numerically examine the effect of a hybrid nanofluid with $\left(Au - Al_2O_3\ /Blood\right)$. This research study involved cases where artery conditions were a stenosis as well as an aneurysm which made the study more realistic. According to the results of their investigation, the incorporation of Al_2O_3 nanoparticles into the Au-blood nanofluid led to an increase in the temperature of the flow. As noted by the researchers, this temperature enhancement has the potential to be useful in applications such as thermal therapy for the elimination of cancer and tumor cells. Tripathi *et al.* [13] present a simulation model for biomedical drug delivery using unsteady hybrid nanoparticles in overlapping stenotic arteries. The researchers utilized hybrid nanoparticles composed of gold and silver, which were shaped in a spherical form. The main objective of this work is to investigate and analyze the induced magnetic field, heat, and flow phenomena in a stenosed artery for a fluid with variable viscosity. The silver-gold nanoparticles and catheter have been utilized. The FTCS approaches are used to simplify the linked mathematical problems in the present article. Zaman *et al.* [14] provided an in-depth analysis of the role of the effective viscosity of the porous medium for a cross-fluid to employing modified Darcy's law. Additionally, the researchers investigated the significance of the Weissenberg number through the overlapping stenosis with a porous medium. Sharma *et al.* [9] investigated the Reynolds viscosity model for hybrid nanoparticles (gold and alumina oxide) with the inclined magnetic field, radiation, viscous dissipation, entropy generation, heat transfer, Joule heating, and tapered multi-stenosed artery. Additionally, the researchers observed when they solved the model by using the Crank-Nicolson Scheme and demonstrated the figures by MATLAB codes with slip velocity then found a direct correlation between the concentration of Au nanoparticles and velocity profile but an inverse correlation between the concentration of Al_2O_3 and velocity profile. Ahmed *et al.* [15] used Galerkin finite element simulation to study inertial addresses in a peristaltically activated MHD blood flow model in an asymmetric channel with a modest Reynolds number. The major finding is that inflating the Casson fluid parameter causes a modest change in velocity in the centre, whereas vorticity lines remain unaltered. Manchi and Ponalagusamy [11] investigated the pulsatile flow of Sutterby nanofluid in an inclined porous tapering artery stenosis. The study considered the effects of electro-osmotic forces, gold (*Au*) nanoparticles, magnetohydrodynamic forces, periodic body stresses, and arterial wall slip. The Poisson-Boltzmann equation is employed to analyze the phenomena related to applied electric fields, while the Debye-Hückel approximation is utilized when the walls possess a low zeta potential.

Vinita *et al.* [16] presented a mathematical model for the MHD nanofluid in the stretching cylinder using the Runge-Kutta method and shooting technique. Makkar *et al.* [17] studied the bio-convective Casson nanofluid flow using the three dimensional model. This study also focused on the effect of the heat source and gyrotactic microorganisms. Makkar *et al.* [18] analysed the Casson nanofluid with the steady MHD flow. They used the Runge-Kutta Fehlberg (RKF) method for solving the nonlinear model.

A review of the existing literature reveals that most studies on blood flow through stenosed arteries and nanofluid dynamics have primarily focused on simplified geometries, such as symmetric or non-symmetric stenosis, and a conventional focus on velocity, temperature, and concentration profiles. Moreover, while several works consider stenosis with bell-shaped geometry, the elliptical shape of the stenosis with the cylindrical artery remains unexplored. So, the current model considers the chemical reaction parameter in the cylindrical artery. Thus, the novelty of the present work lies in integrating body acceleration, elliptical stenosis geometry, and chemical reaction effects within a comparative framework of copper, alumina oxide, and hybrid nanoparticles, offering a more realistic and innovative contribution to the field of biofluid mechanism and nanofluid application in biomedical engineering.

2. Mathematical formulation of the problem

In this mathematical model, blood is considered to be incompressible, laminar, axisymmetric, fully developed, two-dimensional MHD, and unsteady in the stenosed artery. Here, using the cylindrical coordinate and its representation such as $(\bar{r}_1, \bar{\theta}_1, \bar{z}_1)$ in which $\bar{z}_1$ denotes the axial coordinate, $\bar{\theta}_1$ indicates the circumferential/azimuthal coordinate, and finally, $\bar{r}_1$ variable is designated for the radial coordinate. The axisymmetric flow disregards the circumferential direction. Moreover, the $B = (B_0, 0, 0)$ indicates a uniform magnetic field and B_0 expresses a constant magnetic field strength. The stenosis is considered to be elliptical [1-2], and it is described in the mathematical equation and graphically in Fig.1 as:

$$\bar{R}(\bar{z}) = \begin{cases} \bar{R}_0 - \bar{\delta}_s \sin\left[\dfrac{\pi(\bar{z}_1 - \bar{d})}{\bar{L}_0}\right]; & \bar{d} \le \bar{z}_1 \le \bar{d} + \bar{L}_0, \\ \bar{L}_0; & \text{otherwise.} \end{cases}$$

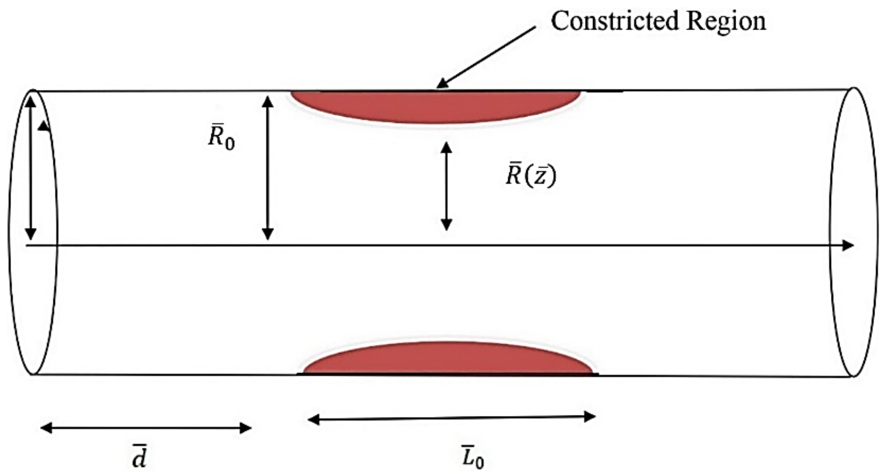

Fig.1. Stenosed artery.

The temperature and velocity for the present model due to axisymmetric and unsteady hybrid nanoparticle-doped blood flow are defined as:

$$\bar{T} = \bar{T}(\bar{r}_1, \bar{z}_1, \bar{t}_1), \quad \bar{V} = [\bar{u}_1, \bar{u}_2, \bar{u}_3], \quad \bar{u}_1 = \bar{u}_1(\bar{r}_1, \bar{z}_1, \bar{t}_1), \quad \bar{u}_2 = \bar{u}_2(\bar{r}_1, \bar{z}_1, \bar{t}_1), \quad \bar{u}_3 = \bar{u}_3(\bar{r}_1, \bar{z}_1, \bar{t}_1),$$

where, $\bar{u}_2(\bar{r}_1, \bar{z}_1, \bar{t}_1) = 0$, $\bar{u}_1, \bar{u}_2, \bar{u}_3$ are the velocities in $\bar{r}_1$, $\bar{\theta}_1$, and $\bar{z}_1$ directions respectively.

The flow equations in mathematical form in terms of hybrid nanoparticles [3, 4, 13, 14, 19, 20, 21] can be written as:

Continuity equation

$$\frac{\partial \bar{u}_1}{\partial \bar{r}_1} + \frac{\bar{u}_1}{\bar{r}_1} + \frac{\partial \bar{u}_3}{\partial \bar{z}_1} = 0. \tag{2.1}$$

Momentum equation in $\bar{r}_1$ direction:

$$\rho_{hnf}\left[\frac{\partial\bar{u}_1}{\partial\bar{t}_1}+\bar{u}_1\frac{\partial\bar{u}_1}{\partial\bar{r}_1}+\bar{u}_3\frac{\partial\bar{u}_1}{\partial\bar{z}_1}\right]=-\frac{\partial\bar{P}_1}{\partial\bar{r}_1}+\frac{1}{\bar{r}_1}\frac{\partial}{\partial\bar{r}_1}\left[\mu_{hnf}\left(\bar{T}\right)\frac{\partial\bar{u}_1}{\partial\bar{r}_1}\right]+ \\ +\frac{\partial}{\partial\bar{z}_1}\left[\mu_{hnf}\left(\bar{T}\right)\left(\frac{\partial\bar{u}_1}{\partial\bar{z}_1}+\frac{\partial\bar{u}_3}{\partial\bar{r}_1}\right)\right]-2\mu_{hnf}\left(\bar{T}\right)\frac{\bar{u}_1}{\bar{r}_1^2}. \tag{2.2}$$

Momentum equation in $\bar{z}_1$ direction:

$$\rho_{hnf}\left[\frac{\partial\bar{u}_3}{\partial\bar{t}_1}+\bar{u}_1\frac{\partial\bar{u}_3}{\partial\bar{r}_1}+\bar{u}_3\frac{\partial\bar{u}_3}{\partial\bar{z}_1}\right]=-\frac{\partial\bar{P}_2}{\partial\bar{z}_1}+\frac{1}{\bar{r}_1}\frac{\partial}{\partial\bar{r}_1}\left[\bar{r}_1\mu_{hnf}\left(\bar{T}\right)\left(\frac{\partial\bar{u}_1}{\partial\bar{z}_1}+\frac{\partial\bar{u}_3}{\partial\bar{r}_1}\right)\right]+ \\ +\frac{\partial}{\partial\bar{z}_1}\left[2\mu_{hnf}\left(\bar{T}\right)\frac{\partial\bar{u}_3}{\partial\bar{z}_1}\right]+(\rho\gamma)_{hnf}\left(\bar{T}-\bar{T}_1\right)g+(\rho\gamma)_{hnf}\left(\bar{C}-\bar{C}_1\right)g-\sigma_{hnf}B_0^2\bar{u}_3+\bar{G}\left(\bar{t}_1\right). \tag{2.3}$$

Energy equation:

$$\left(\rho c_p\right)_{hnf}\left[\frac{\partial\bar{T}}{\partial\bar{t}_1}+\bar{u}_1\frac{\partial\bar{T}}{\partial\bar{r}_1}+\bar{u}_3\frac{\partial\bar{T}}{\partial\bar{z}_1}\right]=(\kappa)_{hnf}\left[\frac{\partial^2\bar{T}}{\partial\bar{r}_1^2}+\frac{1}{\bar{r}_1}\frac{\partial\bar{T}}{\partial\bar{r}_1}+\frac{\partial^2\bar{T}}{\partial\bar{z}_1^2}\right]+\beta_0 \tag{2.4}$$

Concentration equation:

$$\left[\frac{\partial\bar{C}}{\partial\bar{t}_1}+\bar{u}_1\frac{\partial\bar{C}}{\partial\bar{r}_1}+\bar{u}_3\frac{\partial\bar{C}}{\partial\bar{z}_1}\right]=D_c\left[\frac{\partial^2\bar{C}}{\partial\bar{r}_1^2}+\frac{1}{\bar{r}_1}\frac{\partial\bar{C}}{\partial\bar{r}_1}+\frac{\partial^2\bar{C}}{\partial\bar{z}_1^2}\right]-R_c\left(\bar{C}-\bar{C}_1\right) \tag{2.5}$$

The physical properties of hybrid nanoparticles in Eqs (2.1)-(2.5) as ρ_{hnf} is the density, γ_{hnf} is the thermal expansion coefficient, μ_{hnf} is the viscosity, $\bar{G}(\bar{t}_1)$ is the body acceleration term, σ_{hnf} is the electrical conductivity, R_c is the chemical reaction term, g is gravity β_0 is the heat generation parameter, κ_{hnf} is the thermal conductivity, D_c is the mass diffusivity term, $\bar{C}$ is the concentration, $\bar{t}_1$ is time, and $\left(c_p\right)_{hnf}$ is the specific heat.

Initial conditions [1-4]:

$$\bar{u}_3\big|_{\bar{t}_1=0}=0,\ \bar{T}\big|_{\bar{t}_1=0}=0,\ \bar{C}\big|_{\bar{t}_1=0}=0. \tag{2.6}$$

Boundary conditions:

$$\left.\frac{\partial\bar{u}_3}{\partial\bar{r}_1}\right|_{\bar{r}_1=0}=0,\quad \bar{u}_3\big|_{\bar{r}_1=\bar{R}}=0,\quad \left.\frac{\partial\bar{T}}{\partial\bar{r}_1}\right|_{\bar{r}_1=0}=0,\quad \bar{T}\big|_{\bar{r}_1=\bar{R}}=\bar{T}_w,\quad \left.\frac{\partial\bar{C}}{\partial\bar{r}_1}\right|_{\bar{r}_1=0}=0,\quad \bar{C}\big|_{\bar{r}_1=\bar{R}}=\bar{C}_w. \tag{2.7}$$

The axial component of the external periodic body acceleration [22] when $\bar{A}_0$ is the amplitude of body acceleration, χ is the phase angle, $\bar{\omega}_b$ is the frequency of body acceleration then $\bar{G}(\bar{t}_1)$ on the flow of hybrid nano blood is designated by:

$$\bar{G}(\bar{t}_1) = \bar{A}_0 \cos(2\pi\bar{\omega}_b\bar{t}_1 + \chi).$$

To obtain the final numerical solution, it is necessary to transform the aforementioned flow equations, stenosis geometry, initial, and boundary conditions into dimensionless form. The mathematical model is rendered dimensionless by incorporating the subsequent parameters [1-2, 9-10, 22-28]:

$$r = \frac{\bar{r}_1}{\bar{R}_0},\quad t_1 = \frac{\bar{t}_1 U_0}{\bar{R}_0},\quad u_3 = \frac{\bar{u}_3}{U_0},\quad z_1 = \frac{\bar{z}_1}{l_0},\quad \theta = \frac{\bar{T} - \bar{T}_1}{\bar{T}_w - \bar{T}_1},\quad R(z_1) = \frac{\bar{R}(\bar{z}_1)}{\bar{R}_0},\quad \phi = \frac{\bar{C} - \bar{C}_1}{\bar{C}_w - \bar{C}_1},$$

$$\beta = \frac{\bar{R}_0^2 \beta_0}{\left(\bar{T}_w - \bar{T}_1\right)\kappa_f},\quad M^2 = \frac{\sigma_f}{\mu_0}\bar{R}_0^2 \bar{B}_0^2,\quad G_c = \frac{(\rho\gamma)_f\, g\bar{R}_0^2\left(\bar{C}_w - \bar{C}_1\right)}{U_0\mu_0},\quad \xi = \frac{R_c \rho_f \bar{R}_0^2}{\mu_0} \tag{2.8}$$

$$G_r = \frac{(\rho\gamma)_f\, g\bar{R}_0^2\left(\bar{T}_w - \bar{T}_1\right)}{U_0\mu_0},\quad P_r = \frac{\left(c_p\right)_f \mu_0}{\kappa_f},\quad u_1 = \frac{l_0\bar{u}_1}{U_0\delta^*},\quad Re = \frac{\rho_f U_0 \bar{R}_0}{\mu_0},\quad Sc = \frac{\mu_0}{\rho_f D_c}.$$

Using the assumptions from Sharma *et al.* [9] for fully developed flow, mild stenosis $\left(\delta^* \ll 1\right)$ with $O(1) = \varepsilon = \dfrac{\bar{R}_0}{l_0}$, and Eqs (2.1)-(2.7) are modified to use the non-dimensional parameters mentioned in Eq.(2.8):

$$\delta\left(\frac{\partial u_1}{\partial r_1} + \frac{u_1}{r_1}\right) + \frac{\partial u_3}{\partial z_1} = 0\,, \tag{2.9}$$

$$\begin{aligned}\left(\frac{\rho_{hnf}}{\rho_f}\right)Re\,\varepsilon^2\delta\left[\frac{\partial u_1}{\partial t_1} + \delta\varepsilon u_1\frac{\partial u_1}{\partial r_1} + \varepsilon u_3\frac{\partial u_1}{\partial z_1}\right] &= -\frac{\partial P_1}{\partial r_1} + \frac{\delta\bar{R}_0}{l_0^2\mu_0}\frac{1}{r_1}\frac{\partial}{\partial r_1}\left[\mu_{hnf}(\theta)\frac{\partial u_1}{\partial r_1}\right] + \\ &+ \frac{\varepsilon^2\bar{R}_0}{\mu_0}\frac{\partial}{\partial z_1}\left[\mu_{hnf}(\theta)\left(\frac{\delta\varepsilon}{l_0}\frac{\partial u_1}{\partial z_1} + \frac{1}{\bar{R}_0}\frac{\partial u_3}{\partial r_1}\right)\right] - 2\delta\varepsilon^2\frac{\mu_{hnf}(\theta)}{\mu_0}\frac{u_1}{r_1^2},\end{aligned} \tag{2.10}$$

$$\begin{aligned}\left(\frac{\rho_{hnf}}{\rho_f}\right)Re\left[\frac{\partial u_3}{\partial t_1} + \delta\varepsilon u_1\frac{\partial u_3}{\partial r_1} + \varepsilon u_3\frac{\partial u_3}{\partial z_1}\right] &= -\frac{\partial P_2}{\partial z_1} + \frac{1}{r_1}\frac{\partial}{\partial r_1}\left[r_1\frac{\mu_{hnf}(\theta)}{\mu_0}\left(\delta\varepsilon^2\frac{\partial u_1}{\partial z_1} + \frac{\partial u_3}{\partial r_1}\right)\right] + \\ &+ \varepsilon^2\frac{\partial}{\partial z_1}\left[2\frac{\mu_{hnf}(\theta)}{\mu_0}\frac{\partial u_3}{\partial z_1}\right] + \frac{(\rho\gamma)_{hnf}}{(\rho\gamma)_f}G_r\theta + \frac{(\rho\gamma)_{hnf}}{(\rho\gamma)_f}G_c\phi - \frac{\sigma_{hnf}}{\sigma_f}M^2 u_3 + A_1\cos(\omega t_1 + \chi),\end{aligned} \tag{2.11}$$

where $A_1 = \dfrac{\bar{R}_0^2}{U_0\mu_0}\bar{A}_0$ and $\omega = \dfrac{2\pi\bar{\omega}_b\bar{R}_0}{U_0}$.

$$\frac{\left(\rho c_p\right)_{hnf}}{\left(\rho c_p\right)_f}\frac{\kappa_f}{\kappa_{hnf}}PrRe\left[\frac{\partial\theta}{\partial t_1} + \delta\varepsilon u_1\frac{\partial\theta}{\partial r_1} + \varepsilon u_3\frac{\partial\theta}{\partial z_1}\right] = \left[\frac{\partial^2\theta}{\partial r_1^2} + \frac{1}{r_1}\frac{\partial\theta}{\partial r_1} + \varepsilon^2\frac{\partial^2\theta}{\partial z_1^2}\right] + \frac{\kappa_f}{\kappa_{hnf}}\beta, \tag{2.12}$$

$$Re\,Sc\left[\frac{\partial\phi}{\partial t_1}+\delta\varepsilon u_1\frac{\partial\phi}{\partial r_1}+\varepsilon u_3\frac{\partial\phi}{\partial z_1}\right]=\frac{\partial^2\phi}{\partial r_1^2}+\frac{1}{r_1}\frac{\partial\phi}{\partial r_1}+\varepsilon^2\frac{\partial^2\phi}{\partial z_1^2}-Sc\,\xi\,\phi \tag{2.13}$$

The following forms of equations are obtained by employing the condition of fully developed flow and mild stenosis from Sharma *et al.* [9] to Eqs (2.9)-(2.13).

Continuity equation:

$$\frac{\partial u_3}{\partial z_1}=0\,. \tag{2.14}$$

Momentum equation r_1 direction:

$$\frac{\partial P_1}{\partial r_1}=0\,. \tag{2.15}$$

Momentum equation z_1 direction:

$$\begin{aligned}&\left(\frac{\rho_{hnf}}{\rho_f}\right)Re\left[\frac{\partial u_3}{\partial t_1}\right]=-\frac{\partial P_2}{\partial z_1}+\frac{1}{r_1}\frac{\partial}{\partial r_1}\left[r_1\frac{\mu_{hnf}(\theta)}{\mu_0}\frac{\partial u_3}{\partial r_1}\right]+\frac{(\rho\gamma)_{hnf}}{(\rho\gamma)_f}G_r\,\theta+\frac{(\rho\gamma)_{hnf}}{(\rho\gamma)_f}G_c\phi+\\&-\frac{\sigma_{hnf}}{\sigma_f}M^2u_3+A_1\cos(\omega t_1+\chi).\end{aligned} \tag{2.16}$$

Energy equation:

$$\frac{(\rho c_p)_{hnf}}{(\rho c_p)_f}\frac{\kappa_f}{\kappa_{hnf}}\Pr Re\frac{\partial\theta}{\partial t_1}=\frac{\partial^2\theta}{\partial r_1^2}+\frac{1}{r_1}\frac{\partial\theta}{\partial r_1}+\frac{\kappa_f}{\kappa_{hnf}}\beta\,. \tag{2.17}$$

Concentration equation:

$$Re\,Sc\frac{\partial\phi}{\partial t_1}=\frac{\partial^2\phi}{\partial r_1^2}+\frac{1}{r_1}\frac{\partial\phi}{\partial r_1}-Sc\,\xi\,\phi\,. \tag{2.18}$$

Here, we take into account the temperature-dependent viscosity by employing the Reynolds viscosity model used by Tripathi *et al.* [13] which is expressed as $\mu_f(\theta)=\mu_0 e^{-\eta_0\theta}$, where $\eta_0 \ll 1$ and η_0 express the viscosity constant.

The pulsatile hemodynamic impact is simulated using Tripathi *et al.* [13] by including an oscillating pressure gradient when A_0 is the amplitude of the steady state, $\bar{\omega}_p$ is the frequency of the heart pulse, $2\pi\bar{\omega}_p$ is the angular frequency, and A_0' is the amplitude of the pulsatile component of the pressure gradient, as follows:

$$-\frac{\partial\bar{P}_2}{\partial\bar{z}_1}=A_0+A_0'\cos\left(2\pi\bar{\omega}_p\bar{t}_1\right).$$

The dimensionless form of the pressure gradient is expressed as:

$$-\frac{\partial P_2}{\partial z_1} = B_1\left[1 + e\cos\left(c_1 t_1\right)\right], \tag{2.19}$$

where $e = \frac{A_0^{'}}{A_0}$, $B_1 = \frac{A_0 \bar{R}_0^2}{\mu_0 U_0}$, $c_1 = \frac{2\pi \bar{R}_0\, \omega_p}{U_0}$,

Initials and boundary conditions:

$$\begin{gathered} u_3\big|_{t_1=0} = 0, \quad \theta\big|_{t_1=0} = 0, \quad \phi\big|_{t_1=0} = 0, \quad \left.\frac{\partial u_3}{\partial r_1}\right|_{r_1=0} = 0, \\ u_3\big|_{r_1=R_0} = 0, \quad \left.\frac{\partial \theta}{\partial r_1}\right|_{r_1=0} = 0, \quad \theta\big|_{r_1=R_0} = 1, \quad \left.\frac{\partial \phi}{\partial r_1}\right|_{r_1=0} = 0, \quad \phi\big|_{r_1=R_0} = 1. \end{gathered} \tag{2.20}$$

To achieve a rectangular domain for minimizing the geometrical effects, it is necessary to apply the radial transformation $x = \frac{r_1}{R\left(z_1\right)}$ on the geometry being considered. After using the specified transformation, Eqs (2.14)-(2.18) are modified in the following way:

$$\begin{aligned} &\left(\frac{\rho_{hnf}}{\rho_f}\right) Re\left[\frac{\partial u_3}{\partial t_1}\right] = A_1\cos\left(\omega t_1 + \chi\right) + B_1\left[1 + e\cos\left(c_1 t_1\right)\right] + \\ &-\frac{\eta_0}{R^2\left(1-\phi_{Cu}\right)^{2.5}\left(1-\phi_{Al_2O_3}\right)^{2.5}}\left(\frac{\partial u_3}{\partial x}\frac{\partial \theta}{\partial x}\right) + \\ &+\frac{1-\eta_0\theta}{R^2\left(1-\phi_{Cu}\right)^{2.5}\left(1-\phi_{Al_2O_3}\right)^{2.5}}\left[\frac{\partial^2 u_3}{\partial x^2} + \frac{1}{x}\frac{\partial u_3}{\partial x}\right] + \frac{(\rho\gamma)_{hnf}}{(\rho\gamma)_f} G_r\,\theta + \frac{(\rho\gamma)_{hnf}}{(\rho\gamma)_f} G_c\phi - \frac{\sigma_{hnf}}{\sigma_f} M^2 u_3, \end{aligned} \tag{2.21}$$

$$\frac{\left(\rho c_p\right)_{hnf}}{\left(\rho c_p\right)_f}\frac{\kappa_f}{\kappa_{hnf}} \Pr Re\frac{\partial \theta}{\partial t_1} = \frac{1}{R^2}\left(\frac{\partial^2\theta}{\partial x^2} + \frac{1}{x}\frac{\partial \theta}{\partial x}\right) + \frac{\kappa_f}{\kappa_{hnf}}, \tag{2.22}$$

$$Re\,Sc\frac{\partial \phi}{\partial t_1} = \frac{1}{R^2}\left(\frac{\partial^2\phi}{\partial x^2} + \frac{1}{x}\frac{\partial \phi}{\partial x}\right) - Sc\,\xi\,\phi\,. \tag{2.23}$$

The initials and boundary conditions specified in Eq. (2.20) are obtained after applying the radial coordinate transformation:

$$u_3\big|_{t_1=0} = 0, \quad \theta\big|_{t_1=0} = 0, \quad \phi\big|_{t_1=0} = 0, \quad \left.\frac{\partial u_3}{\partial x}\right|_{x=0} = 0, \tag{2.24}$$

$$u_3\big|_{x=1}=0,\quad \left.\frac{\partial\theta}{\partial x}\right|_{0=0}=0,\quad \theta\big|_{x=1}=1,\quad \left.\frac{\partial\phi}{\partial x}\right|_{x=0}=0,\quad \phi\big|_{x=1}=1. \tag{2.24 cont.}$$

The author's work on WSS, heat transfer rate (Nusselt number), mass transfer rate (Sherwood number) in the artery, and follows these concepts according to Sharma *et al*. [10] as follows:

$$\tau_\omega=-\frac{1}{R}\left(\frac{\partial u_3}{\partial x}\right)_{x=1}, \tag{2.25}$$

$$Sh=-\frac{1}{R}\left(\frac{\partial\phi}{\partial x}\right)_{x=1}, \tag{2.26}$$

$$Nu=-\frac{1}{R}\left(\frac{\partial\theta}{\partial x}\right)_{x=1}. \tag{2.27}$$

The volumetric flow rate [9] for the artery is defined as:

$$Q=2\pi R^2\left(\int_0^1 u_3 x\,dx\right). \tag{2.28}$$

3. Solution of the problem

There are many well-recognized numerical methods available for solving partial differential equations.

Table 1. Thermophysical properties of copper nanofluid.

Properties	Mathematical expression for copper nanofluid (cylindrical shape of nanoparticles) [9-10, 13-14, 30-31,]
Viscosity	$\mu_{nf}=\dfrac{\mu_f(\theta)}{(1-\phi_{Cu})^{2.5}}$
Density	$\rho_{nf}=(1-\phi_{Cu})\rho_f+\phi_{Cu}\rho_{Cu}$
Heat capacity	$(\rho c_p)_{nf}=(1-\phi_{Cu})(\rho c_p)_f+\phi_{Cu}(\rho c_p)_{Cu}$
Thermal expansion coefficient	$\dfrac{(\rho\gamma)_{nf}}{(\rho\gamma)_f}=(1-\phi_{Cu})+\phi_{Cu}\dfrac{(\rho\gamma)_{Cu}}{(\rho\gamma)_f}$
Thermal conductivity	$\dfrac{\kappa_{nf}}{\kappa_f}=\dfrac{\kappa_{Cu}+3.9\kappa_f-3.9\phi_{Cu}(\kappa_f-\kappa_{Cu})}{\kappa_{Cu}+3.9\kappa_f+\phi_{Cu}(\kappa_f-\kappa_{Cu})}$
Electrical conductivity	$\dfrac{\sigma_{nf}}{\sigma_f}=\dfrac{\sigma_{Cu}+3.9\sigma_f-3.9\phi_{Cu}(\sigma_f-\sigma_{Cu})}{\sigma_{Cu}+3.9\sigma_f+\phi_{Cu}(\sigma_f-\sigma_{Cu})}$

Obtaining the exact solution or analytical solution of the transformed nonlinear partial differential equations is complicated. Therefore, it is required to employ numerical methods for solving the non-linear partial differential equations from Eqs (2.21)-(2.23). Hoffmann and Chiang [29] provide a detailed description of the FTCS algorithm, an explicit finite-difference technique that is suitable for solving these equations based on the discretization of PDEs. Moreover, other researchers have used this method in their research. The procedure begins by discretizing the spatial domain. Then, for each x_i at the time instant $(t_1)_k$, the value of the velocity component $u_3 = (u_3)_{(i,k)}$, temperature $\theta = \theta_{(i,\, k)}$, and concentration $\phi =, \phi_{(i,\, k)}$ are determined respectively. Now, the velocity component's numerical value is computed at each discretized point at the time instant $(t_1)_k$. The value of $(t_1)_k$ is defined as $(k-1)\Delta t_1$, where Δt_1 denotes the time step or small increment in time. The stability of this approach depends upon the values of Δx and Δt_1. Thus, in order to satisfy the stability requirement of the numerical solution, the following step sizes are selected. The change in x is 0.025 and the change in t_1 is 0.0001. More information on this method's stability and convergence can be found in Hoffmann and Chiang book [29].

Using the FTCS scheme in Eqs (2.21)-(2.23) and after apply the equations become as:

$$\begin{aligned}
\theta_{(i,k+1)} &= \theta_{(i,\,k)} + \frac{(\rho c_p)_f}{(\rho c_p)_{hnf}} \frac{\kappa_{hnf}}{\kappa_f} \frac{\Delta t_1}{\Pr Re} \frac{1}{R^2} \frac{1}{(\Delta x)^2} \theta_{(i+1,k)} + \\
&- 2\frac{(\rho c_p)_f}{(\rho c_p)_{hnf}} \frac{\kappa_{hnf}}{\kappa_f} \frac{\Delta t_1}{\Pr Re} \frac{1}{R^2} \frac{1}{(\Delta x)^2} \theta_{(i,k)} + \frac{(\rho c_p)_f}{(\rho c_p)_{hnf}} \frac{\kappa_{hnf}}{\kappa_f} \times \\
&\times \frac{\Delta t_1}{\Pr Re} \frac{1}{R^2} \frac{1}{(\Delta x)^2} \theta_{(i-1,k)} + \frac{(\rho c_p)_f}{(\rho c_p)_{hnf}} \frac{\kappa_{hnf}}{\kappa_f} \frac{\Delta t_1}{\Pr Re} \frac{1}{R^2} \frac{1}{x_{(i)} 2\Delta x} \theta_{(i+1,k)} + \\
&- \frac{(\rho c_p)_f}{(\rho c_p)_{hnf}} \frac{\kappa_{hnf}}{\kappa_f} \frac{\Delta t_1}{\Pr Re} \frac{1}{R^2} \frac{1}{x_{(i)} 2\Delta x} \theta_{(i-1,k)} + \frac{(\rho c_p)_f}{(\rho c_p)_{hnf}} \frac{\Delta t_1}{\Pr Re} \beta,
\end{aligned} \tag{3.1}$$

$$\begin{aligned}
\phi_{(i,k+1)} &= \phi_{(i,\,k)} + \frac{\Delta t_1}{Re Sc} \frac{1}{R^2} \frac{1}{(\Delta x)^2} \phi_{(i+1,k)} - 2\frac{\Delta t_1}{Re Sc} \frac{1}{R^2} \frac{1}{(\Delta x)^2} \phi_{(i,k)} + \frac{\Delta t_1}{Re Sc} \frac{1}{R^2} \frac{1}{(\Delta x)^2} \phi_{(i-1,k)} + \\
&\frac{\Delta t_1}{Re Sc} \frac{1}{R^2} \frac{1}{x_{(i)} 2\Delta x} \phi_{(i+1,k)} - \frac{\Delta t_1}{Re Sc} \frac{1}{R^2} \frac{1}{x_{(i)} 2\Delta x} \phi_{(i-1,k)} - \frac{\Delta t_1}{Re} \xi \phi_{(i,\,k)}.
\end{aligned} \tag{3.2}$$

The equations formulated by Devi and Devi [30] are employed to compute the thermophysical properties of copper and alumina oxide nanofluid, in addition to the hybrid nanofluid composed of copper and alumina oxide.

$$\begin{aligned}
(u_3)_{(i,k+1)} &= (u_3)_{(i,\,k)} + \left(\frac{\rho_f}{\rho_{hnf}}\right) \frac{\Delta t_1}{Re} A_1 \cos\left(\omega (k-1)\Delta t_1 + \chi\right) + \\
&+ \left(\frac{\rho_f}{\rho_{hnf}}\right) \frac{\Delta t_1}{Re} B_1 \left[1 + e\cos\left(c_1 (k-1)\Delta t_1\right)\right] +
\end{aligned} \tag{3.3}$$

$$-\left(\frac{\rho_f}{\rho_{hnf}}\right)\frac{\Delta t_1}{Re}\frac{\eta_0}{R^2\left(1-\phi_{Cu}\right)^{2.5}\left(1-\phi_{Al_2O_3}\right)^{2.5}}\frac{1}{4\left(\Delta x\right)^2}\times$$
$$\left[\left(u_3\right)_{(i+1,k)}\left(u_3\right)_{(i+1,k)}-\left(u_3\right)_{(i+1,k)}\theta_{(i-1,k)}-\left(u_3\right)_{(i-1,k)}\left(u_3\right)_{(i+1,k)}+\left(u_3\right)_{(i-1,k)}\theta_{(i-1,k)}\right]+$$
$$+\left(\frac{\rho_f}{\rho_{hnf}}\right)\frac{\Delta t_1}{Re}\frac{1-\eta_0\theta_{(i,k)}}{R^2\left(1-\phi_{Cu}\right)^{2.5}\left(1-\phi_{Al_2O_3}\right)^{2.5}}\frac{1}{\left(\Delta x\right)^2}\left(u_3\right)_{(i+1,k)}+$$
$$-2\left(\frac{\rho_f}{\rho_{hnf}}\right)\frac{\Delta t_1}{Re}\frac{1-\eta_0\theta_{(i,k)}}{R^2\left(1-\phi_{Cu}\right)^{2.5}\left(1-\phi_{Al_2O_3}\right)^{2.5}}\frac{1}{\left(\Delta x\right)^2}\left(u_3\right)_{(i,k)}+$$
$$+\left(\frac{\rho_f}{\rho_{hnf}}\right)\frac{\Delta t_1}{Re}\frac{1-\eta_0\theta_{(i,k)}}{R^2\left(1-\phi_{Cu}\right)^{2.5}\left(1-\phi_{Al_2O_3}\right)^{2.5}}\frac{1}{\left(\Delta x\right)^2}\left(u_3\right)_{(i-1,k)}+ \qquad (3.3\text{ cont.})$$
$$+\left(\frac{\rho_f}{\rho_{hnf}}\right)\frac{\Delta t_1}{Re}\frac{1-\eta_0\theta_{(i,k)}}{R^2\left(1-\phi_{Cu}\right)^{2.5}\left(1-\phi_{Al_2O_3}\right)^{2.5}}\frac{1}{x_{(i)}2\Delta x}\left(u_3\right)_{(i+1,k)}+$$
$$-\left(\frac{\rho_f}{\rho_{hnf}}\right)\frac{\Delta t_1}{Re}\frac{1-\eta_0\theta_{(i,k)}}{R^2\left(1-\phi_{Cu}\right)^{2.5}\left(1-\phi_{Al_2O_3}\right)^{2.5}}\frac{1}{x_{(i)}2\Delta x}\left(u_3\right)_{(i-1,k)}+$$
$$+\left(\frac{\rho_f}{\rho_{hnf}}\right)\frac{\Delta t_1}{Re}\frac{(\rho\gamma)_{hnf}}{(\rho\gamma)_f}G_r\,\theta_{(i,\,k)}+\left(\frac{\rho_f}{\rho_{hnf}}\right)\frac{\Delta t_1}{Re}\frac{(\rho\gamma)_{hnf}}{(\rho\gamma)_f}G_c\phi_{(i,\,k)}+$$
$$-\left(\frac{\rho_f}{\rho_{hnf}}\right)\frac{\Delta t_1}{Re}\frac{\sigma_{hnf}}{\sigma_f}M^2\left(u_3\right)_{(i,\,k)}.$$

Table 2. Thermophysical properties of copper, alumina oxide nanofluid and blood, its values [13].

Properties	Blood	Copper	Alumina Oxide
Density	*1063*	*8933*	*3970*
Heat capacity	*3594*	*385*	*765*
Thermal expansion coefficient	*0.18*	*1.67*	*0.85*
Thermal conductivity	*0.492*	*400*	*40*
Electrical conductivity	6.67×10^{-1}	5.96×10^{7}	3.5×10^{7}

Table 3. Thermophysical properties of alumina oxide nanofluid [9-10, 13-14, 30-31].

Properties	Mathematical expression for Alumina Oxide nanofluid (cylindrical shape of nanoparticles)
Viscosity	$\mu_{nf}=\dfrac{\mu_f(\theta)}{\left(1-\phi_{Al_2O_3}\right)^{2.5}}$

Table 3 cont. Thermophysical properties of alumina oxide nanofluid [9-10, 13-14, 30-31].

Properties	Mathematical expression for Alumina Oxide nanofluid (cylindrical shape of nanoparticles)
Density	$\rho_{nf} = \left(1-\phi_{Al_2O_3}\right)\rho_f + \phi_{Al_2O_3}\rho_{Al_2O_3}$
Heat capacity	$\left(\rho c_p\right)_{nf} = \left(1-\phi_{Al_2O_3}\right)\left(\rho c_p\right)_f + \phi_{Al_2O_3}\left(\rho c_p\right)_{Al_2O_3}$
Thermal expansion coefficient	$\dfrac{(\rho\gamma)_{nf}}{(\rho\gamma)_f} = \left(1-\phi_{Al_2O_3}\right) + \phi_{Al_2O_3}\dfrac{(\rho\gamma)_{Al_2O_3}}{(\rho\gamma)_f}$
Thermal conductivity	$\dfrac{\kappa_{nf}}{\kappa_f} = \dfrac{\kappa_{Al_2O_3} + 3.9\kappa_f - 3.9\phi_{Al_2O_3}\left(\kappa_f - \kappa_{Al_2O_3}\right)}{\kappa_{Al_2O_3} + 3.9\kappa_f + \phi_{Al_2O_3}\left(\kappa_f - \kappa_{Al_2O_3}\right)}$
Electrical conductivity	$\dfrac{\sigma_{nf}}{\sigma_f} = \dfrac{\sigma_{Al_2O_3} + 3.9\sigma_f - 3.9\phi_{Al_2O_3}\left(\sigma_f - \sigma_{Al_2O_3}\right)}{\sigma_{Al_2O_3} + 3.9\sigma_f + \phi_{Al_2O_3}\left(\sigma_f - \sigma_{Al_2O_3}\right)}$

Table 4. Thermophysical properties of copper and alumina oxide nanofluid [9-10, 13-14, 30-31].

Properties	Mathematical expression for hybrid nanofluid (cylindrical shape of hybrid nanoparticles)
Viscosity	$\mu_{hnf} = \dfrac{\mu_f(\theta)}{\left(1-\phi_{Al_2O_3}\right)^{2.5}\left(1-\phi_{Cu}\right)^{2.5}}$
Density	$\rho_{hnf} = \left(1-\phi_{Al_2O_3}\right)\left[\left(1-\phi_{Cu}\right)\rho_f + \phi_{Cu}\rho_{Cu}\right] + \phi_{Al_2O_3}\rho_{Al_2O_3}$
Heat capacity	$\left(\rho c_p\right)_{hnf} = \left(1-\phi_{Al_2O_3}\right)\left[\left(1-\phi_{Cu}\right)\left(\rho c_p\right)_f + \phi_{Cu}\left(\rho c_p\right)_{Cu}\right] + \phi_{Al_2O_3}\left(\rho c_p\right)_{Al_2O_3}$
Thermal expansion coefficient	$\dfrac{(\rho\gamma)_{hnf}}{(\rho\gamma)_f} = \left(1-\phi_{Al_2O_3}\right)\left[\left(1-\phi_{Cu}\right) + \phi_{Cu}\dfrac{(\rho\gamma)_{Cu}}{(\rho\gamma)_f}\right] + \phi_{Al_2O_3}\dfrac{(\rho\gamma)_{Al_2O_3}}{(\rho\gamma)_f}$
Thermal conductivity	$\dfrac{\kappa_{hnf}}{\kappa_f} = \left[\dfrac{\kappa_{Al_2O_3} + 3.9\kappa_{nf} - 3.9\phi_{Al_2O_3}\left(\kappa_{nf} - \kappa_{Al_2O_3}\right)}{\kappa_{Al_2O_3} + 3.9\kappa_{nf} + \phi_{Al_2O_3}\left(\kappa_{nf} - \kappa_{Al_2O_3}\right)}\right]\left[\dfrac{\kappa_{Cu} + 3.9\kappa_f - 3.9\phi_{Cu}\left(\kappa_f - \kappa_{Cu}\right)}{\kappa_{Cu} + 3.9\kappa_f + \phi_{Cu}\left(\kappa_f - \kappa_{Cu}\right)}\right]$
Electrical conductivity	$\dfrac{\sigma_{hnf}}{\sigma_f} = \left[\dfrac{\sigma_{Al_2O_3} + 3.9\sigma_{nf} - 3.9\phi_{Al_2O_3}\left(\sigma_{nf} - \sigma_{Al_2O_3}\right)}{\sigma_{Al_2O_3} + 3.9\sigma_{nf} + \phi_{Al_2O_3}\left(\sigma_{nf} - \sigma_{Al_2O_3}\right)}\right]\left[\dfrac{\sigma_{Cu} + 3.9\sigma_f - 3.9\phi_{Cu}\left(\sigma_f - \sigma_{Cu}\right)}{\sigma_{Cu} + 3.9\sigma_f + \phi_{Cu}\left(\sigma_f - \sigma_{Cu}\right)}\right]$

4. Results and discussion

This section addresses the impact of various flow-related parameters on non-dimensional velocity, non-dimensional temperature, non-dimensional concentration, wall shear stress, flow rate, Nusselt number, and Sherwood number. These parameters include the volume fractions of copper nanoparticles, volume fractions of alumina oxide nanoparticles, volume fractions of hybrid nanoparticles, magnetic field, Reynolds number, thermal Grashof number, and solutal Grashof number. The dimensionless governing equations have been simplified using the FTCS method. The FTCS method is implemented in MATLAB to calculate profiles of velocity, temperature, concentration, flow rate, Nusselt number, Sherwood number, and wall shear stress. The contours are plotted over time in order to analyze the flow patterns for different physical-influencing variables. Table 1 to 4 illustrates the thermal physical characteristics of blood, gold, and alumina oxide nanoparticles. The computational work was performed by utilizing the default parameter settings, as shown $\phi_{Cu} = 0.01$, $\phi_{Al_2O_3} = 0.01$, $Pr = 14$, $Re = 2$, $\beta = 0.1$, $Sc = 0.5$, $M = 1$, $B_1 = 1.41$, $c_1 = 1$, $\eta_0 = 0.2$, $G_r = 0.1$, $G_c = 0.01$, $\delta = 0.2$ [2, 4, 12-14, 21, 30-35].

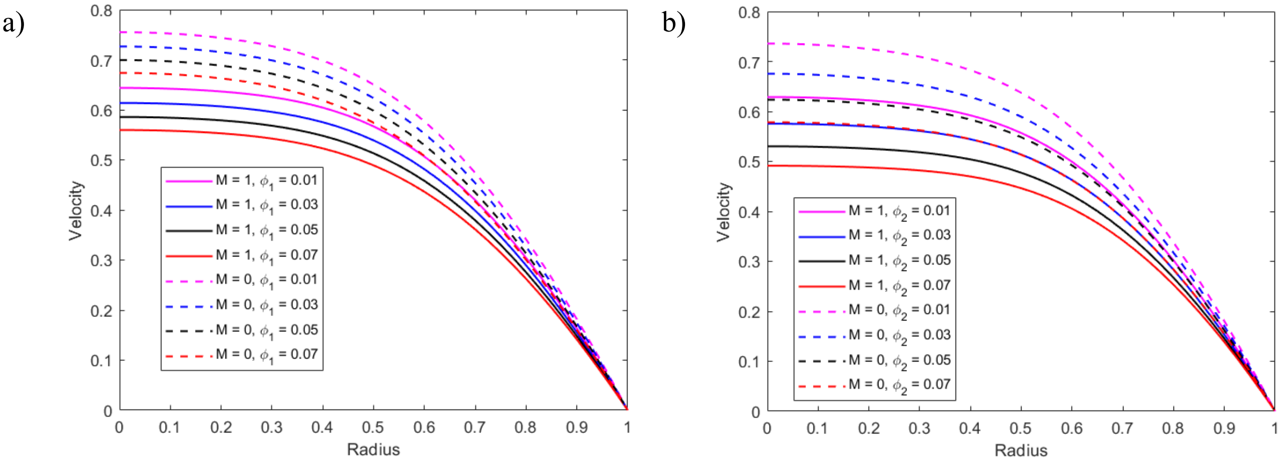

Fig.2. (a) Effect of the cylindrical shape of the copper nanoparticle (ϕ_1) concentration on the axial velocity (u_3): A comparison with and without a magnetic field (M), (b) Effect of the cylindrical shape of alumina oxide nanoparticle (ϕ_2) concentration on the axial velocity (u_3): A comparison with and without a magnetic field (M).

Figure 2(a) illustrates the influence of different concentrations (volume fractions) of copper nanoparticles on the axial blood velocity component, both in the presence and absence of a magnetic field. Figure 2(a) demonstrates that increasing the concentration of copper nanoparticles leads to a noticeable decrease in flow velocity. Furthermore, it is apparent that when a more powerful magnetic field is applied in the radial direction, the maximum velocity is reduced. The Lorentz magnetic drag force restricts the flow of blood and causes deceleration in the narrowed artery. The velocity is highest at the centerline of the artery in this plot and then drops towards the arterial wall, where it reaches zero. Figure 2(b) demonstrates the impact of various concentrations (volume fractions) of alumina oxide nanoparticles on the axial velocity, both with and without a magnetic field. Figure 2(b) illustrates that augmenting the concentration of alumina oxide nanoparticles results in a discernible reduction in flow velocity, albeit at a slower rate compared to copper nanoparticles. Moreover, it is evident that increasing the strength of the magnetic field in the radial direction leads to a decrease in the maximum velocity. The Lorentz magnetic drag force impedes the movement of blood and induces deceleration in the constricted artery. The velocity is maximum at the centerline of the artery in this plot and thereafter decreases towards the arterial wall, where it achieves zero.

The impact of changing hybrid nanoparticle concentrations (volume fractions) on the axial velocity is depicted in Fig.3(a) for both magnetic field presence and absence. Figure 3(a) illustrates that altering the concentration of alumina oxide nanoparticles within the range of 0.01 to 0.07 .Results in a discernible reduction in flow velocity. However, this decrease is more gradual when compared to copper and alumina oxide nanoparticles. Also, the use of a stronger magnetic field in the radial direction leads to a decrease in the maximum velocity. The Lorentz magnetic drag force restricts the flow of blood and causes slowing in the narrowed artery. The velocity reaches its maximum at the centerline of the artery in this plot and subsequently falls towards the arterial wall, until reaching zero. Figure 3(b) illustrates the influence of the presence and absence of a magnetic field on the axial velocity, considering different scenarios: the absence of nanoparticles, the presence of only copper nanoparticles, the presence of only alumina oxide nanoparticles, and the presence of hybrid nanoparticles at varying concentrations (volume fractions). Figure 3(b) demonstrates that applying a magnetic field in the radial direction causes a reduction in the velocity of blood flow in the artery.

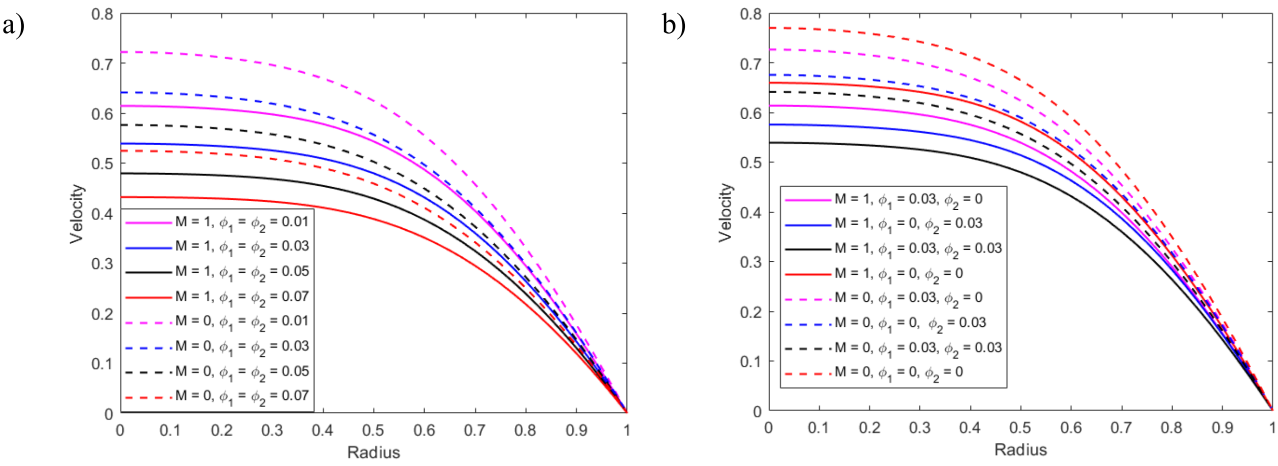

Fig.3. (a) Effect of the cylindrical shape of the hybrid (copper (ϕ_1) and alumina oxide (ϕ_2)) nanoparticle concentration on the axial velocity (u_3): A comparison with and without a magnetic field (M), (b) Effect of magnetic field (M) on axial velocity (u_3): A comparison with blood, copper nanoparticle, alumina oxide nanoparticle, and hybrid (copper (ϕ_1) and alumina oxide (ϕ_2)) nanoparticle.

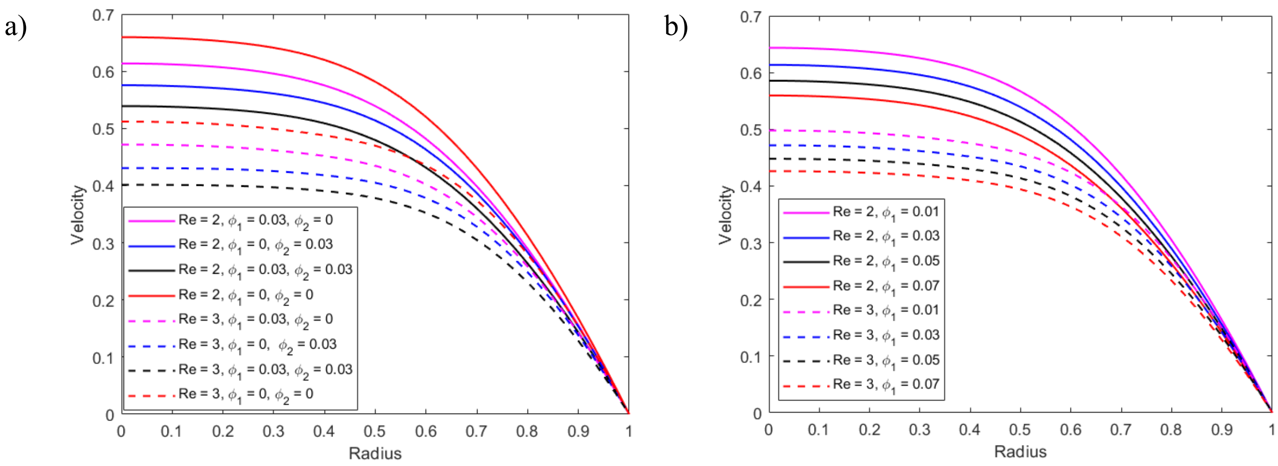

Fig.4. (a) Effect of Reynolds number (Re) on axial velocity (u_3) for blood, copper nanoparticle (ϕ_1), alumina oxide nanoparticle (ϕ_2), and a hybrid (copper and alumina oxide) nanoparticle with different values of Reynolds number ($Re = 2$ and 3), (b) Effect of the cylindrical shape of the copper nanoparticle (ϕ_1) concentration on the axial velocity (u_3) with different values of Reynolds number ($Re = 2$ and 3).

The velocity is greater in the absence of nanoparticles and slower in the presence of hybrid nanoparticles. However, when only copper nanoparticles or only alumina oxide nanoparticles are present, the velocity is intermediate. Figure 4(a) demonstrates the influence of the Reynolds number on the axial velocity, taking into account various scenarios: no nanoparticles, only copper nanoparticles, only alumina oxide nanoparticles, and hybrid nanoparticles at different concentrations (volume fractions). It should be noted that at low Reynolds numbers, the flow is laminar and viscosity is the most effective. The numbers indicate that the value of Re changes 2 to 3 and the velocity reduces significantly. Although the increase in the Reynolds number (which varies with the radius of the vessel) is a factor that leads to the increase in the inertial force, the primary cause of the flow of the blood is the deceleration, created by the stenotic blockage. This causes a great resistance in the blood flow. The flow is greater with the absence of nanoparticles and lesser with the presence of the hybrid nanoparticles. But when copper nanoparticles are added alone, the velocity is intermediate as well as when alumina oxide nanoparticles are added alone. Figure 4(b) demonstrates the effect of various concentrations (volume fractions) of copper nanoparticles on the axial velocity particularly in Reynolds numbers of $Re = 2$ and $Re = 3$. The numerical data shows that the increase in the value of Re whereby Re rises by 2 to 3, a significant reduction in velocity is recorded. The flow decreases with an increase of the concentration of copper nanoparticles. The speed is highest in the center of the artery in the graph and then decreasing to the arterial wall till zero.

In Fig.5(a), the influence of different concentrations (volume fractions) of the nanoparticles of alumina oxide on the axial velocity is plotted, in particular, at the Reynolds number, $Re = 2$ and $Re = 3$. The numerical results show that there is a huge reduction in velocity as the` value of Re increases between 2 to 3. The velocity of the alumina oxide nanoparticles reduces as their concentration rises, and this decrease is more pronounced compared to the decrease in velocity of copper nanoparticles only. Figure 5(b) highlights the effect of various concentrations (volume fractions) of hybrid nanoparticles on the axial velocity, notably at Reynolds numbers $Re = 2$ and 3. The numerical results represent a notable reduction in velocity as the Reynolds number climbs from 2 to 3. As the concentration of the hybrid nanoparticles boosts, their velocity diminishes.

a)

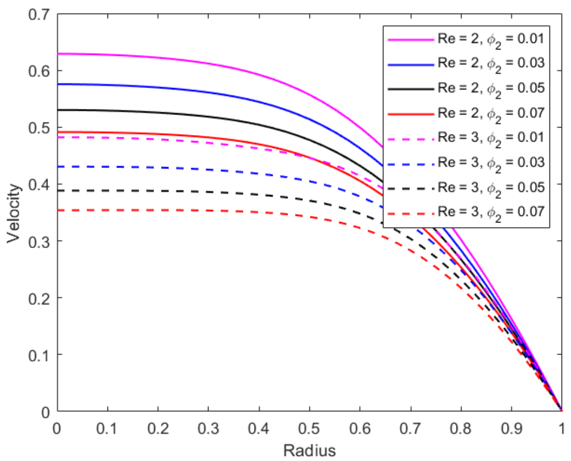

b)

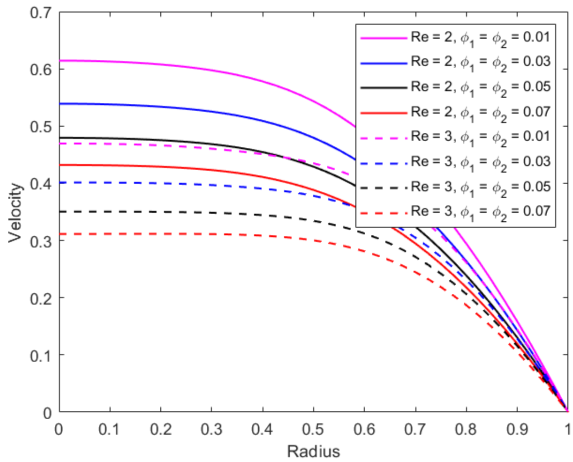

Fig.5. (a) Effect of the cylindrical shape of ϕ_2 concentration on the u_3 with different values of Re ($Re = 2$ and 3), (b) Effect of the cylindrical shape of the hybrid (copper (ϕ_1) and alumina oxide (ϕ_2)) nanoparticle concentration on the u_3 with different values of Re ($Re = 2$ and 3).

Figure 6(a) shows the velocity profile for different thermal Grashof numbers (Gr), taking into account the influence of varied concentrations (volume fractions) of copper nanoparticles. The computational findings demonstrate an obvious rise in velocity when the value of Gr is increasing. The Grashof number (Gr) represents the relationship between the buoyant force and the viscous force in the hemodynamic regime.

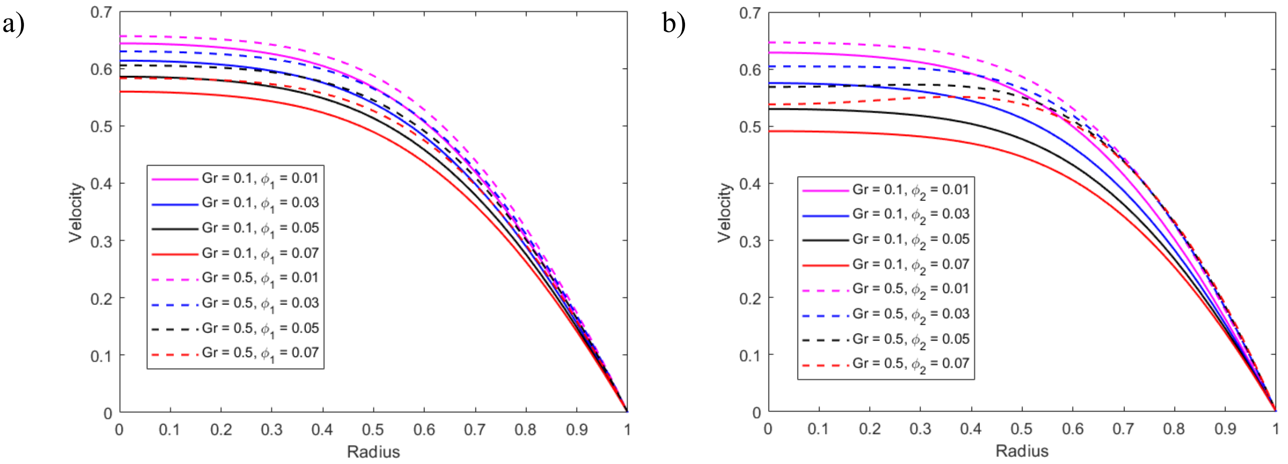

Fig.6. (a) Effect of the cylindrical shape of the ϕ_1 concentration on the u_3 with different values of Gr ($Gr = 0.1$ and 0.5), (b) Effect of the cylindrical shape of ϕ_2 concentration on the u_3 with different values of Gr ($Gr = 0.1$ and 0.5).

It is worth mentioning that a rise in the concentration of copper nanoparticles leads to a restriction in flow. Figure 6(b) exhibits a velocity profile for various thermal Grashof numbers Gr and different concentrations (volume percentages) of alumina oxide nanoparticles. Figure 6(b) depicts a positive correlation between velocity and the growth in the value of Gr. It is important to observe that an increased concentration of alumina oxide nanoparticles results in a reduction in flow.

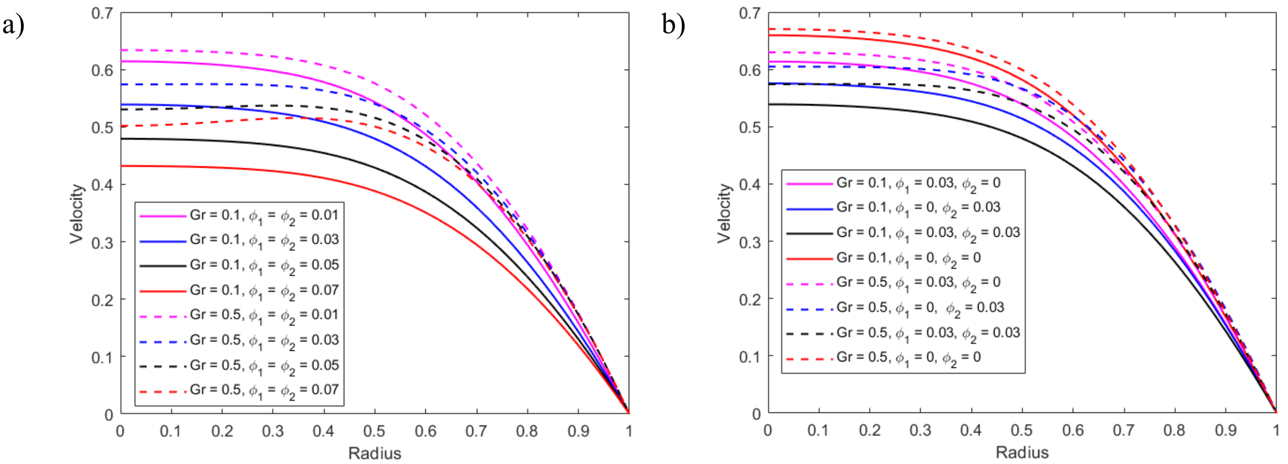

Fig.7. (a) Effect of the cylindrical shape of the hybrid (copper (ϕ_1) and alumina oxide (ϕ_2)) nanoparticle concentration on the u_3 with different values of Gr ($Gr = 0.1$ and 0.5), (b) Effect of Gr on u_3 for blood, ϕ_1, ϕ_2, and hybrid (copper (ϕ_1) and alumina oxide (ϕ_2)) nanoparticle with different values of Gr ($Gr = 0.1$ and 0.5).

Figure 7(a) discloses a velocity profile for varied thermal Grashof number (Gr) and varying concentrations (volume percentages) of hybrid nanoparticles. Figure 7(a) illustrates a direct relationship between velocity and the increase in the value of Gr. It is crucial to note that a higher concentration of hybrid nanoparticles leads to a slump in flow. Figure 7(b) depicts the impact of thermal Grashof numbers (Gr) on the axial velocity, taking into account various scenarios: the absence of nanoparticles, the inclusion of only copper.Nanoparticles, the inclusion of only alumina oxide nanoparticles, and the inclusion of hybrid nanoparticles at different concentrations (volume fractions). It shows that an increase in the thermal Grashof number in the radial direction leads to an acceleration in the velocity of blood flow in the artery. The velocity is higher in the absence of nanoparticles and lower in the presence of hybrid nanoparticles. However, in the presence of either copper nanoparticles or alumina oxide nanoparticles independently, the velocity is at a medium level.

a)

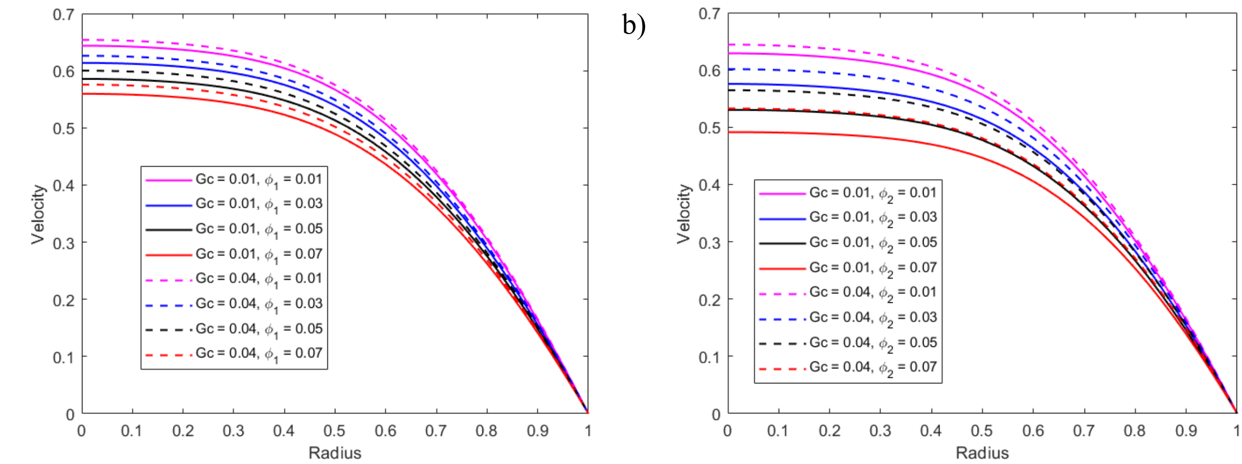

Fig.8. (a) Effect of the cylindrical shape of the copper nanoparticle (ϕ_1) concentration on the axial velocity (u_3) with different values of solutal Grashof number ($Gc = 0.01$ and 0.04), (b) Effect of the cylindrical shape of alumina oxide nanoparticle (ϕ_2) concentration on the axial velocity (u_3) with different values of solutal Grashof number ($Gc = 0.01$ and 0.04).

Figure 8(a) illustrates how the concentration of copper nanoparticles in a cylindrical form affects the velocity in the radial direction. This is observed for various values of the solutal Grashof number, while also considering the velocity of blood in the radial direction. A graphical study reveals that the flow velocity decreases towards zero as the distance from the center line to the arterial wall, referred to as r, varies. The graphic demonstrates that an increase in the solutal Grashof number results in a decrease in viscous force, leading to an increase in flow velocity. Furthermore, it has been noted that a rise in the concentration of copper nanoparticles leads to a decrease in flow. The relation shown is that, the higher the concentration of alumina oxide nanoparticles, the lower the flow is as illustrated in Fig.8.(b). Applying the fluid dynamics, one should mention that the increase of Gc could be accompanied by the improvement of the velocity profile. The higher the Gc parameter, the stronger the force of buoyancy and less the force of viscosity. The resultant effect of this phenomenon is an increase in the convective pattern of flow as shown in Fig.8.(b).

Figure 9(a) shows that the increased concentration of hybrid nanoparticles concurs less flow. With the same figure, the Gc parameter especially 0.01 to 0.04 becomes more prominent compared with the buoyancy force than the viscous forces. Thus, the effect of this process is an enhanced pattern of convectional flow as shown in Fig.9(a). The effect of the solutal Grashof number on the axial velocity of a variety of substances, i.e., blood, copper nanoparticles, alumina oxide nanoparticles and nanoparticles mixing copper and alumina oxide is illustrated in Fig.9.(b). Solutal Grashof number increased by 0.01 to 0.04 and this increases the flow pattern. The flow is higher without the nanoparticles, but it is less with the presence of the hybrid nanoparticles. Velocity is medium when this has copper and alumina oxide nanoparticles.

Figure 10(a) to 11(b) clarifies that the parameter of viscosity influences the axial velocity of the copper nanoparticles, alumina oxide nanoparticles and hybrid nanoparticles. Figure 10(a)-11(a) indicates a decrease in velocity with an increase of concentration of copper nanoparticles (Fig.10(a)) and alumina oxide nanoparticles (Fig.10(b)) and hybrid nanoparticles (Fig.11(a)) respectively.

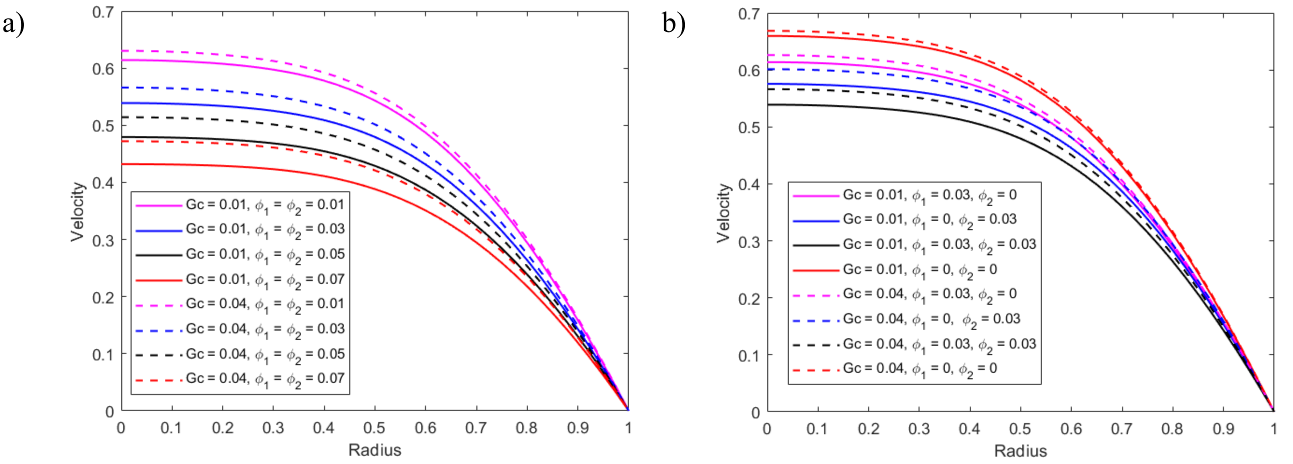

Fig.9. (a) Effect of the cylindrical shape of the hybrid (copper (ϕ_1) and alumina oxide (ϕ_2)) nanoparticle concentration on the u_3 with different values of Gc ($Gc = 0.01$ and 0.04), (b) Effect of Gc on u_3 for blood, copper nanoparticle (ϕ_1), alumina oxide nanoparticle (ϕ_2), and hybrid (copper and alumina oxide) nanoparticle different values of Gc ($Gc = 0.01$ and 0.04).

The high velocity is depicted in Fig.11(b) when the nanoparticle is not present and low when the hybrid nanoparticle is present. Further, the viscosity parameter is directly proportional to the flow. The slower the viscosity parameter the lower the velocity. This is explained by the fact that the viscosity is increased and the resistance to flow is thereby increased resulting in a reduction of the flow velocity.

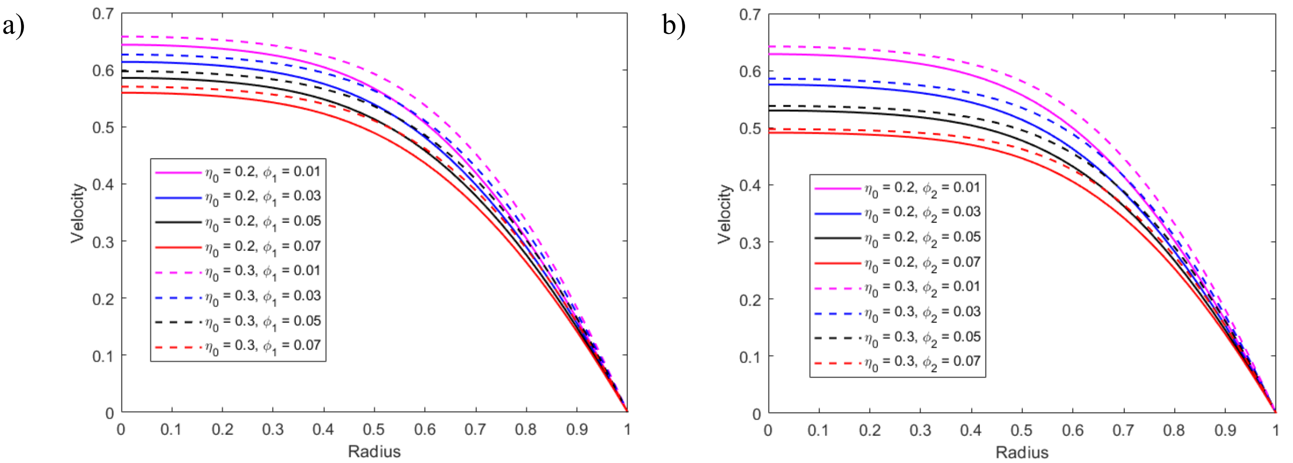

Fig.10. (a) Effect of the cylindrical shape of copper nanoparticle (ϕ_1) concentration on the axial velocity (u_3) with different values of viscosity parameter ($\eta_0 = 0.2$ and $\eta_0 = 0.3$), (b) Effect of the cylindrical shape of alumina oxide nanoparticle (ϕ_2) concentration on the axial velocity (u_3) with different values of viscosity parameter ($\eta_0 = 0.2$ and $\eta_0 = 0.3$).

Figures 12(a) to 13(b) bring out the physiological impact on Prandtl number on the axial velocity of copper nanoparticles, alumina oxide nanoparticles and hybrid nanoparticles. Figures 12 (a) to 13 (a) show that there is a slowing down in velocity with increasing concentration of copper nanoparticles (Fig.12(a)) and those of alumina oxide nanoparticles (Fig.12(b)) and hybrid nanoparticles (Fig.13(a)) respectively.

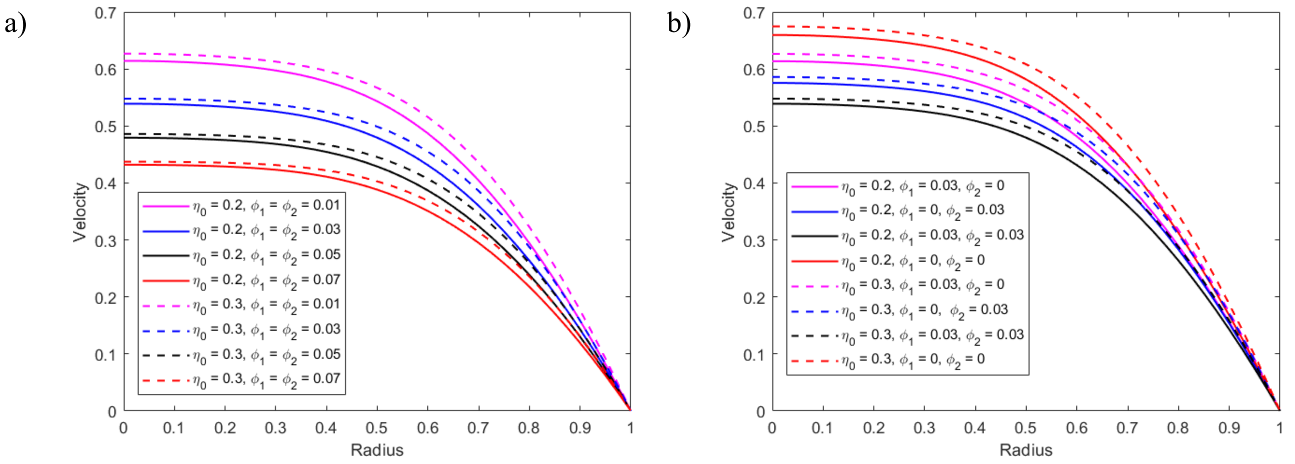

Fig.11. (a) Effect of the cylindrical shape of the hybrid (copper (ϕ_1) and alumina oxide (ϕ_2)) nanoparticle concentration on the axial velocity (u_3) with different values of the viscosity parameter ($\eta_0 = 0.2$ and $\eta_0 = 0.3$), (b) Effect of viscosity parameter (η_0) on axial velocity (u_3) for blood, copper nanoparticle, alumina oxide nanoparticle, and hybrid (copper (ϕ_1) and alumina oxide (ϕ_2)) nanoparticle with different values of the viscosity parameter ($\eta_0 = 0.2$ and $\eta_0 = 0.3$).

The presence of a higher velocity at the absence of the nanoparticle and a lower velocity in the presence of the hybrid nanoparticle are indicated by Fig.13(b). Velocity increases with increasing Pr in a blood flow system, where the Pr is the ratio of the momentum diffusiveness (kinematic viscosity) to the thermal diffusiveness. The higher the Prandtl number, the more probable that the momentum diffusivity dominates over the thermal one, and the more effective the fluid is in terms of the transfer of the momentum instead of the heat. A Prandtl number increases giving a climb to the velocity.

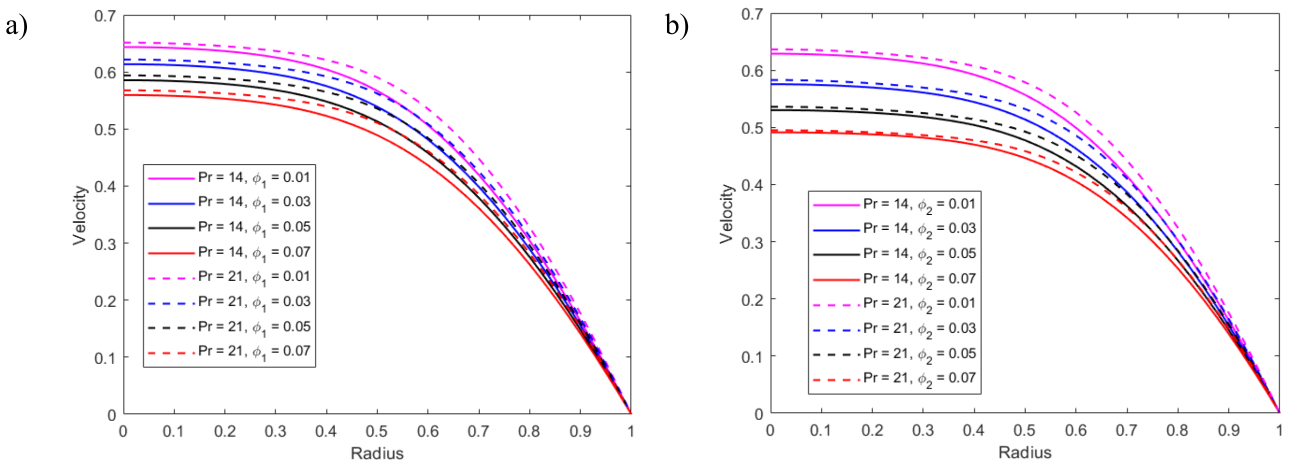

Fig.12. (a) Effect of the cylindrical shape of the copper nanoparticle (ϕ_1) concentration on the axial velocity (u_3) with different values of Prandtl number ($Pr = 14$ and $Pr = 21$), (b) Effect of the cylindrical shape of alumina oxide nanoparticle (ϕ_2) concentration on the axial velocity (u_3) with different values of Prandtl number ($Pr = 14$ and $Pr = 21$).

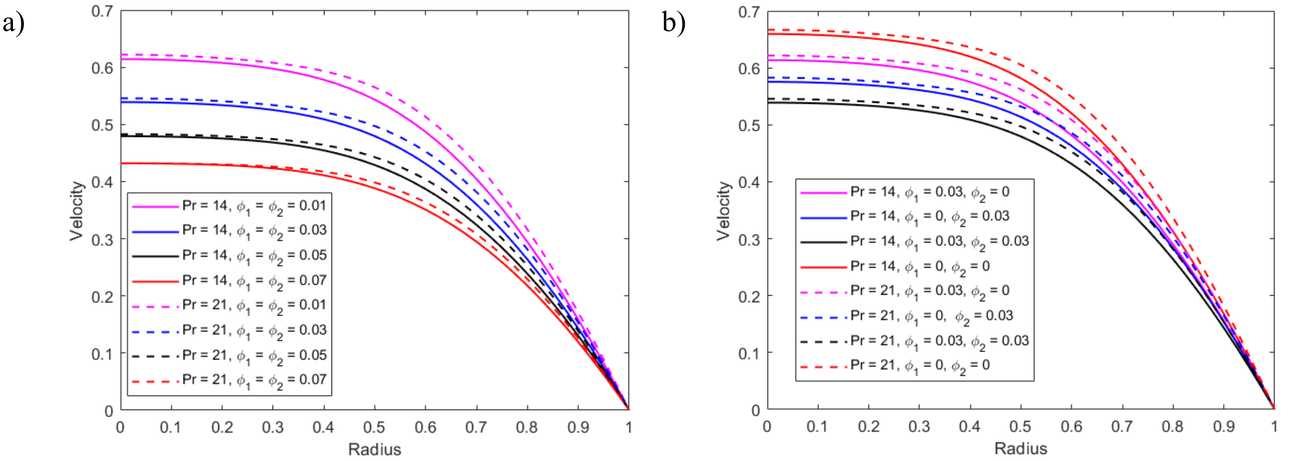

Fig.13. (a) Effect of the cylindrical shape of the hybrid (copper (ϕ_1) and alumina oxide (ϕ_2)) nanoparticle concentration on the axial velocity (u_3) with different values of Prandtl number ($Pr = 14$ and $Pr = 21$), (b) Effect of Prandtl number (Pr) on axial velocity (u_3) for blood, copper nanoparticle (ϕ_1), alumina oxide nanoparticle (ϕ_2), and a hybrid (copper and alumina oxide) nanoparticle with different values of Prandtl number ($Pr = 14$ and $Pr = 21$).

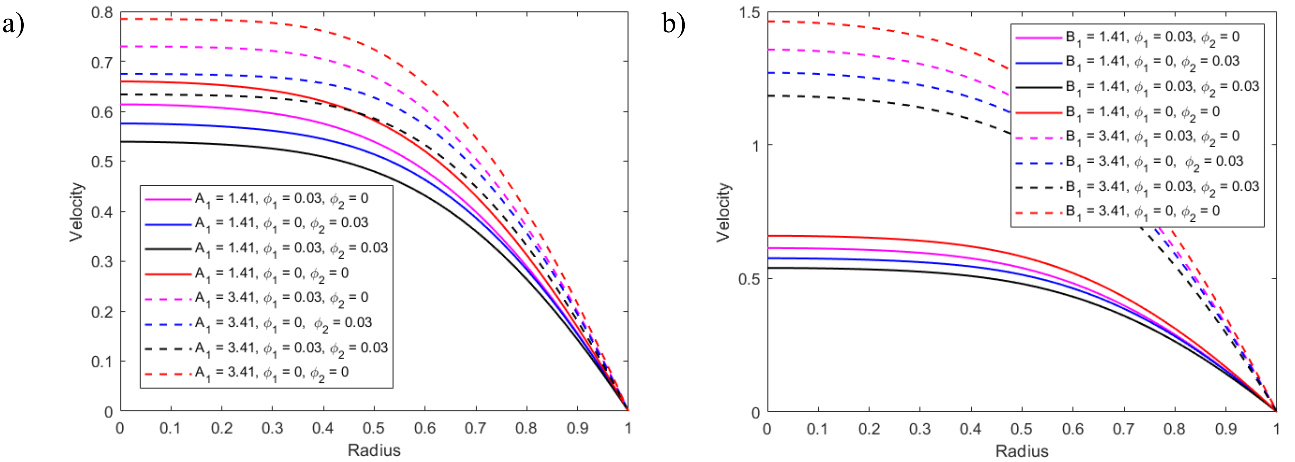

Fig.14. (a) Effect of body acceleration parameter (A_1) on axial velocity (u_3) for blood, copper nanoparticle (ϕ_1), alumina oxide nanoparticle (ϕ_2), and a hybrid (copper and alumina oxide) nanoparticle with different values of body acceleration parameter ($A_1 = 1.41$ and $A_1 = 3.41$), (b) Effect of pressure gradient parameter (B_1) on axial velocity (u_3) for blood, copper nanoparticle (ϕ_1), alumina oxide nanoparticle (ϕ_2), and a hybrid (copper and alumina oxide) nanoparticle with different values of the pressure gradient parameter ($B_1 = 1.41$ and $B_1 = 3.41$).

Figure 14(a) shows the relationship between various levels of body acceleration with the presence of copper, alumina oxide and hybrid nanoparticles in the bloodstream. The higher the level of nanoparticles or hybrid nanoparticles in the blood, the lower the flow will be. The greater the body acceleration parameter then the greater the velocity. The effect of the pulsatile pressure gradient parameter B_1 on the velocity profiles in the constricted artery is shown in Fig.14(b). With increase in B_1 levels, it is evident that blood acceleration during systole also increases. The accelerated rate of movement results in the elevated blood flow in the artery resulting in the increase of velocities. Nanoparticles in the blood reduce blood flow.

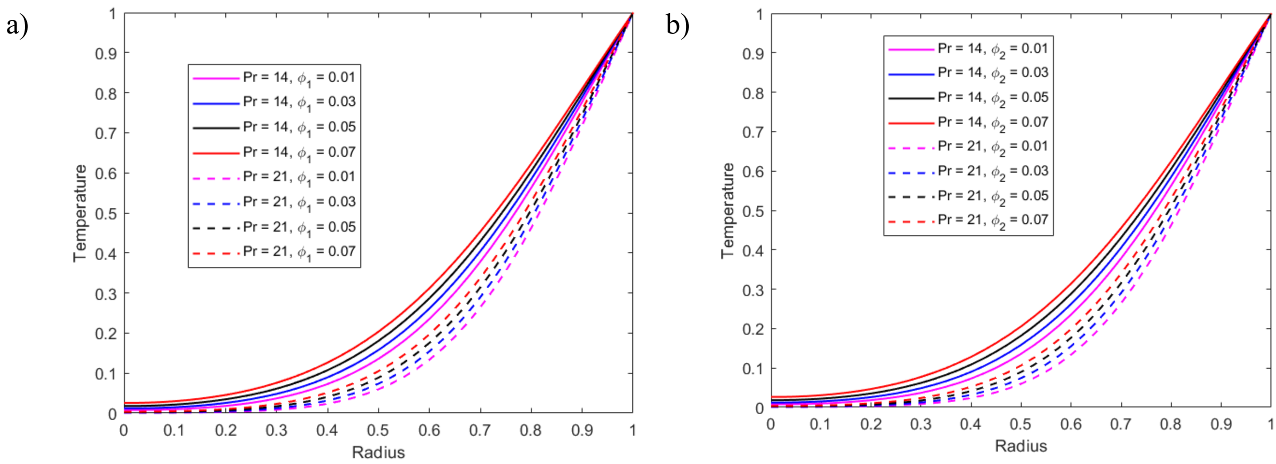

Fig.15. (a) Effect of the cylindrical shape of the copper nanoparticle (ϕ_1) concentration on the temperature profile (θ) with different values of Prandtl number ($Pr = 14$ and $Pr = 21$), (b) Effect of the cylindrical shape of alumina oxide nanoparticle (ϕ_2) concentration on the temperature profile (θ) with different values of Prandtl number ($Pr = 14$ and $Pr = 21$).

The temperature distribution of different Prandtl numbers (Pr) has been plotted in Fig.15(a) by taking into account the influence of various concentrations (volume fractions) of copper nanoparticles. The temperature profile has a direct positive correlation with the copper nanoparticles concentration. The larger the Prandtl number, the more important is the effect of the thermal diffusivity as compared to the momentum diffusivity. In other words, the fluid has increased heat transfer compared to momentum transfer. The development of this particular property is witnessed when one looks at the temperature distribution of the fluid. Figure 15(a) indicates that an increase in the Prandtl number in the range *14* to *21* is accompanied by a drop in temperature profile. This observation means that the fluid proves to have a better ability to transfer momentum which is mainly determined by its flow or movement and not its ability to transfer heat. This in turn causes the flow by which the temperature varies within the fluid, known as the temperature gradient to be less observable. To highlight the significance of the patient difference in concentration (volume fraction) of alumina oxide nanoparticles in the temperature distribution, Fig.15(b) focuses on the temperature distribution of different values of Prandtl numbers (Pr). The concentration of alumina oxide nanoparticles has a positive direct correlation with the temperature profile. Figure 15(b) indicates that during an increase in the Prandtl number between *14* to *21*, the temperature profile decreases.

The temperature field concerning various Prandtl numbers (Pr) taking into account the effect of concentration (volume fractions) of hybrid nanoparticles is shown in Fig.16(a). The hybrid nanoparticles concentration shows a large direct correlation with the temperature profile. In Fig.16(a), it is observed that as the value of the Prandtl number rises between *14* and *21* the temperature profile reduces. Figure 16(b) reveals that the concentration of copper nanoparticles in a cylindrical shape affects the temperature profile at various Reynolds numbers. While the Reynolds number increases, the temperatures decrease, and the profiles become flatter. They become closer to the zero line, and while the temperature increases away from the wall, it does so at greater distances from the center. The presence of copper nanoparticles boosts the temperature distribution.

Figure 17 exhibit similar patterns to Fig.16(b).

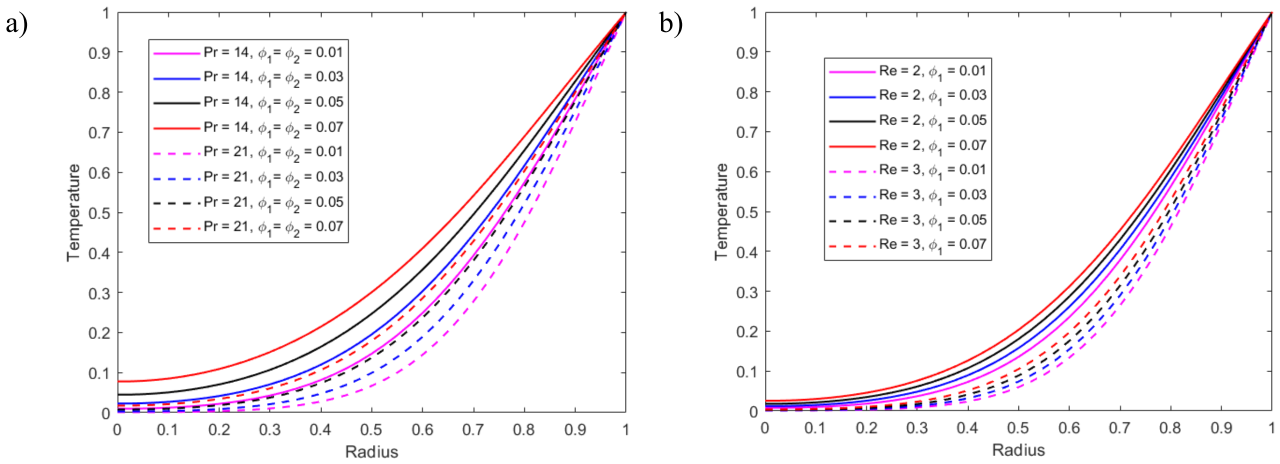

Fig.16. (a) Effect of the cylindrical shape of the hybrid (copper (ϕ_1) and alumina oxide (ϕ_2)) nanoparticle concentration on the temperature profile (θ) with different values of Prandtl number ($Pr = 14$ and $Pr = 21$), (b) Effect of the cylindrical shape of the copper nanoparticle (ϕ_1) concentration on the temperature profile (θ) with different values of Reynolds number ($Re = 2$ and $Re = 3$).

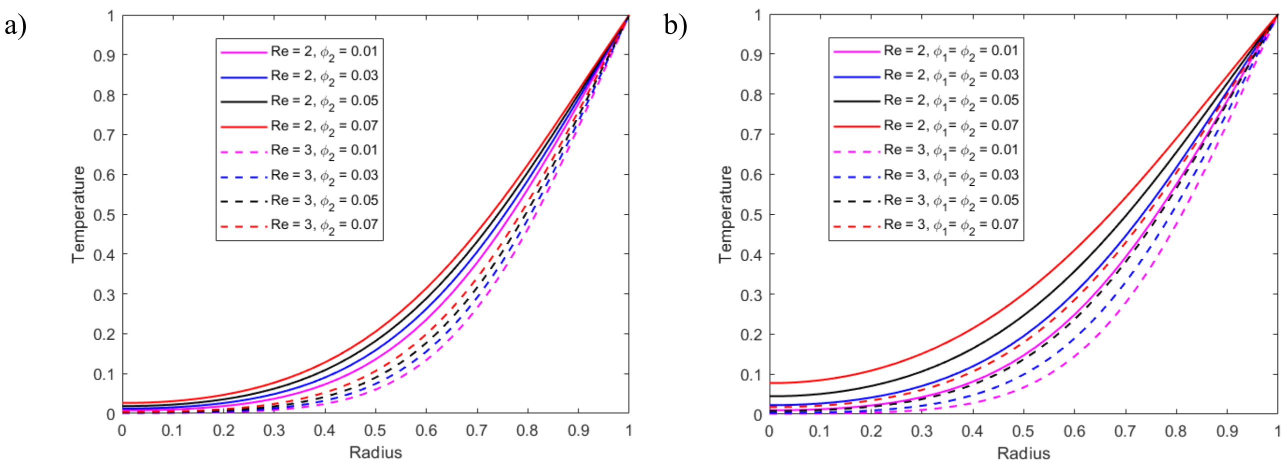

Fig.17. (a) Effect of the cylindrical shape of alumina oxide nanoparticle (ϕ_2) concentration on the temperature profile (θ) with different values of Reynolds number ($Re = 2$ and $Re = 3$), (b) Effect of the cylindrical shape of the hybrid (copper (ϕ_1) and alumina oxide (ϕ_2)) nanoparticle concentration on the temperature profile (θ) with different values of Reynolds number ($Re = 2$ and $Re = 3$).

Figure 18(a) portrays the concentration profile in the blood that is shown to rise as the Schmidt number grows within the range of 0.5 to 2. A higher Sc value implies that the rate of mass transfer is relatively faster than the rate of momentum transfer. The observed phenomena suggest that the fluid's ability to transmit momentum through convection or flow is more significant than its ability to transport mass or concentration. Figure 18(b) displays the concentration distribution of the Reynolds number throughout the range of 2 to 5. The concentration profile decreases as the Reynolds number increases.

Figure 19(a) depicts the time series plots of wall shear stress in the stenosed artery as the thermal Grashof number varies, while considering the presence of nanoparticles. If we increase the value of the thermal Grashof number, it can be noted in the figure that the wall shear stress increases.

a)

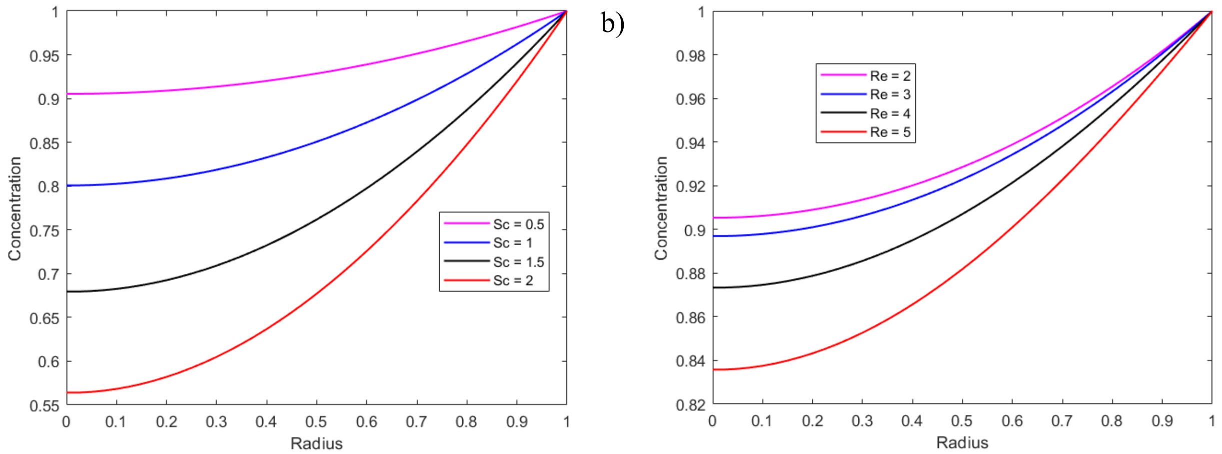

Fig.18. (a) Effect of Schmidt number (Sc) on the concentration profile (ϕ) with different values of Schmidt number ($Sc = 0.5, 1, 1.5$ and 2), (b) Effect of Reynolds number (Re) on the concentration profile (ϕ) with different values of Reynolds number ($Re = 2, 3, 4$ and $Re = 5$).

a)

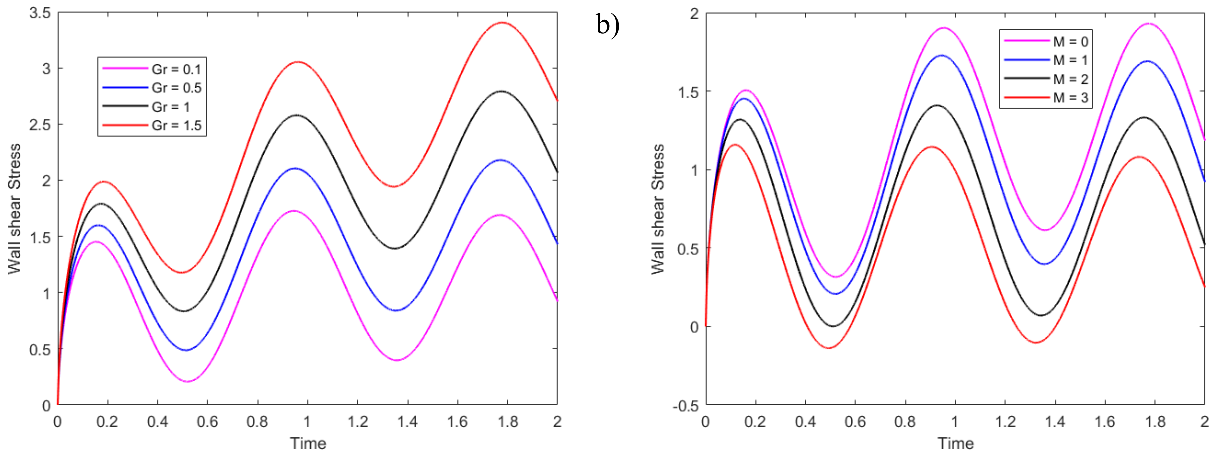

Fig.19. (a) Effect of Gr on the WSS with different values of Gr ($Gr = 0.1, 0.5, 1$ and $Gr = 1.5$), (b) Effect of the M on the WSS with different values of the M ($M = 0, 1, 2$ and $M = 3$).

The graph exhibits oscillations as a result of pulsating. Figure 19(b) illustrates the temporal changes in wall shear stress through the fluctuations in the magnetic field. As the magnetic field strength is raised, the wall shear stress diminishes, and when the magnetic field is lowered to zero, the wall shear stress reaches its maximum level. The wall shear stress in graph 20(a) is depicted by the correlation between the Reynolds number and the time series change. With an increase in the Reynolds number, there is a corresponding drop in the wall shear stress, which exhibits a sinusoidal behavior. The highest variation occurs when the Reynolds number is low. The Reynolds number experiences minimal variation in the adjacency layer of the flow when it is low. The downturn in Reynolds number results in a transition towards a more laminar flow. The global maxima and global minima are occurring exclusively at low Reynolds numbers.

The patterns of wall shear stress for varying nanoparticle concentrations and Prandtl number (Pr) values are shown in Figs 20(b)-21(a), respectively. The wall shear stresses in Fig.20(b) exhibit a positive association with the Prandtl number, but a negative correlation with the hybrid nanoparticle concentration. A higher Prandtl number results in an elevation of the wall shear stress. Moreover, the nature of WSS resembles that of the sine function, exhibiting an increase in amplitude in both figures.

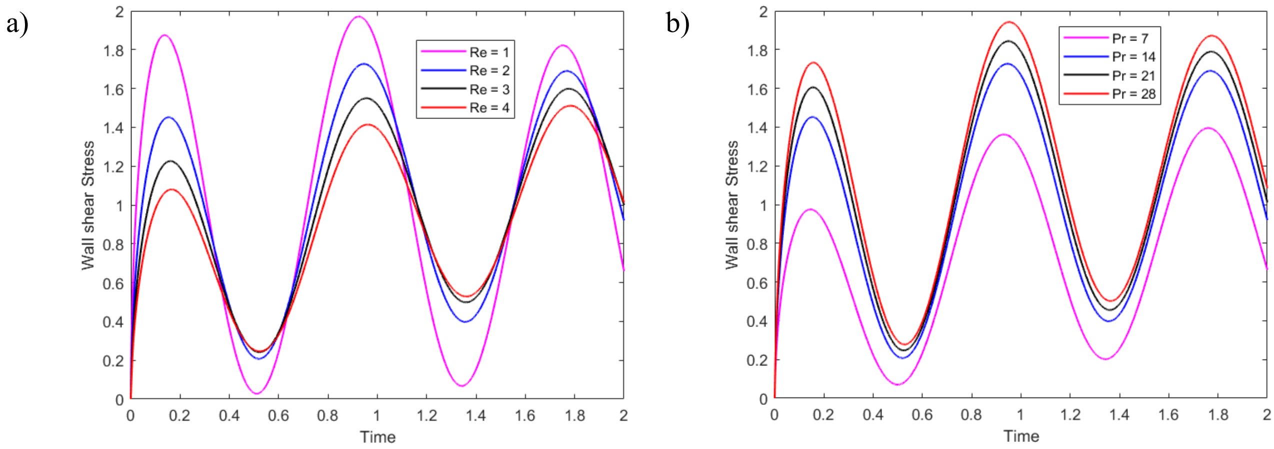

Fig.20. (a) Effect of Re on the WSS with different values of Re ($Re = 1, 2, 3, 4$), (b) Effect of Pr on the WSS with different values of Pr ($Pr = 7, 14, 21, 28$).

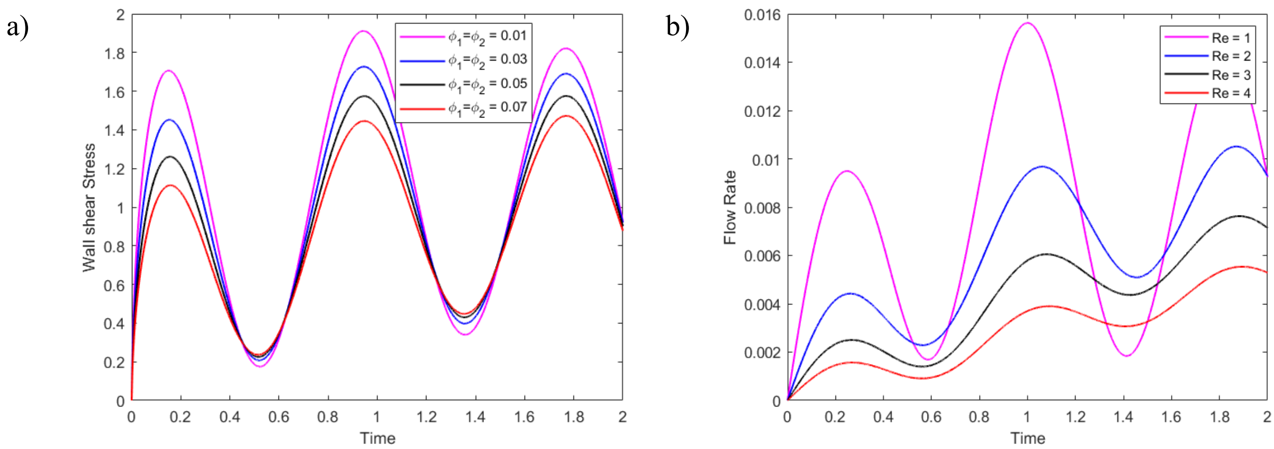

Fig.21. (a) Effect of the cylindrical shape of the hybrid (copper (ϕ_1) and alumina oxide (ϕ_2)) nanoparticles on the wall shear stress, (b) Effect of Re on the VFR with different values of Re $(Re = 1, 2, 3, 4)$.

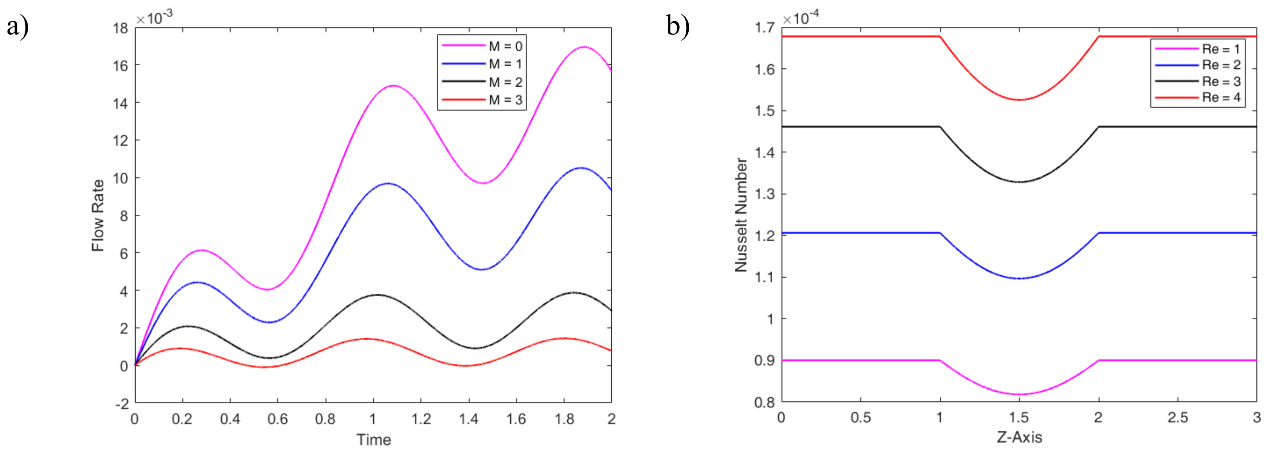

Fig.22. (a) Effect of M on the VFR with different values of the M $(M = 0, 1, 2, 3)$, (b) Effect of Re on Nu with different values of Re $(Re = 1, 2, 3, 4)$.

Figures 21(b) and 22(a) illustrate the variation of the volumetric flow rate as the Reynolds number Re and the magnetic field parameter (M) increase, respectively. strongly periodic profiles are once again calculated across a broad variety of time intervals. In Fig.22(a), there is a noticeable decrease in flow rate as the magnetic fields increase. Therefore, by increasing the Lorentzian body force, a significant decrease in hemodynamic acceleration is achieved. While higher Reynolds numbers do result in more inertial effects, the primary consequence observed in Fig.21(b) is the slowing down of the flow and reduced flux.

Figures 22(b) and 23(a) represent the Nusselt number as it varies with the Reynolds number and Prandtl number, respectively. The Nusselt number (Nu) is a nondimensional metric employed in the fields of fluid dynamics and heat transport. The term refers to the proportion of convective heat transfer compared to conductive heat transfer over a boundary layer of fluid. From Figs 22(b)-23(a), we detected a decrease in trends with increasing Reynolds and Prandtl values, respectively.

Figure 23(b) highlights the relationship between the Sherwood number and the Schmidt number. The Sherwood number is directly influenced by the Schmidt number, especially in situations where mass transfer is predominantly governed by diffusion. When the Schmidt number is elevated, signifying reduced mass diffusion, the Sherwood number typically declines. The reason for this is that a greater Schmidt number leads to the formation of larger concentration boundary layers, which subsequently decrease the rate of mass transfer across the boundary layer.

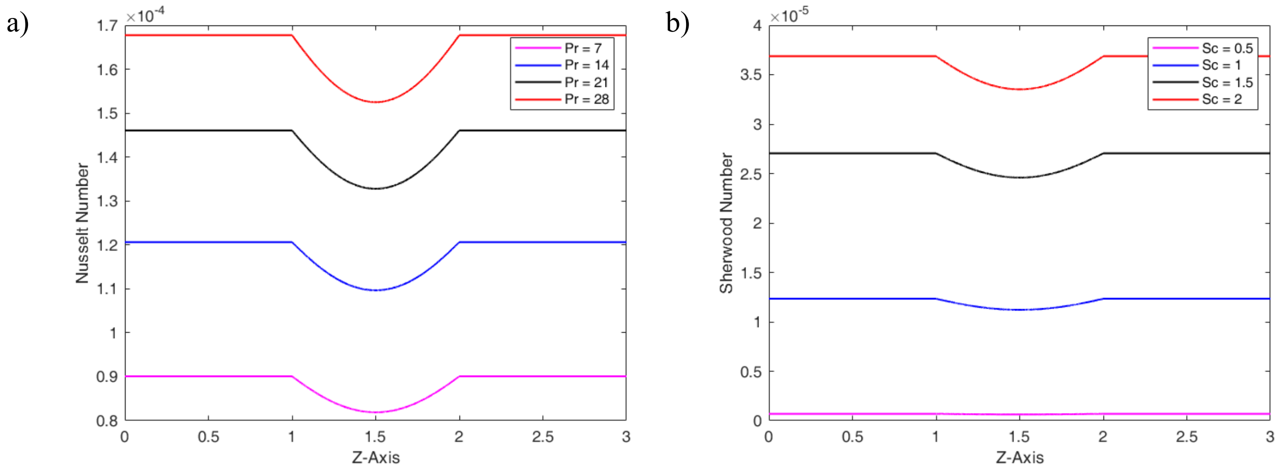

Fig.23. (a) Effect of Pr on Nu with different values of Pr $(Pr = 7, 14, 21, 28)$, (b) Effect of Sc on Sh with different values of Sc $(Sc = 0.5, 1, 1.5, 2)$.

Figure 24 shows the velocity contour over time with various values of the dimensionless parameter. In Fig.24(a) represents the impact of the magnetic field $(M = 1)$, Fig.24(b) absence of magnetic field $(M = 0)$, Fig.24(c) Reynolds number $(Re = 3)$, Fig.24(d) thermal Grashof number $(Gr = 0.5)$, Fig.24.(e) Solutal Grashof number $(Gc = 0.04)$, Fig.24.(f) viscosity parameter $(\eta_0 = 0.3)$, Fig.24(g) Prandtl number $(Pr = 21)$, Fig.24(h) Body acceleration parameter $(A_1 = 3.14)$, Fig.24(i) pressure gradient parameter $(B_1 = 3.14)$, and Fig.24(j) concentration of hybrid nanoparticles (0.05) on the velocity contour over time.

In Figs 24(a)-24(b) on changing the magnetic parameter from 1 to 0, the bolus size decreases, but along the time axis maximum value is attained when $M = 0$. On increases Re, the inner boluses decrease in Fig.24(c). In Fig.24(d) increase Gr, the inner boluses are approximately stable but positively increment over time. In Fig.24.(e) on changing Gc from 0.02 to 0.04, the inner bolus size increases but in Fig.24(f), when η_0 increase it is stable. From Fig.24(h), it is observed that near the arterial wall flow increases. Figures 24(i) and 24(j), in both patterns of boluses are changed, and the maximum value is close to 1 in Fig.24(i) but declines in Fig.24(j). Figures 25(a), (b), and (c) show the concentration contour over time for different physical parameters of Reynolds number 2, 3, and Schmidt number 2, respectively.

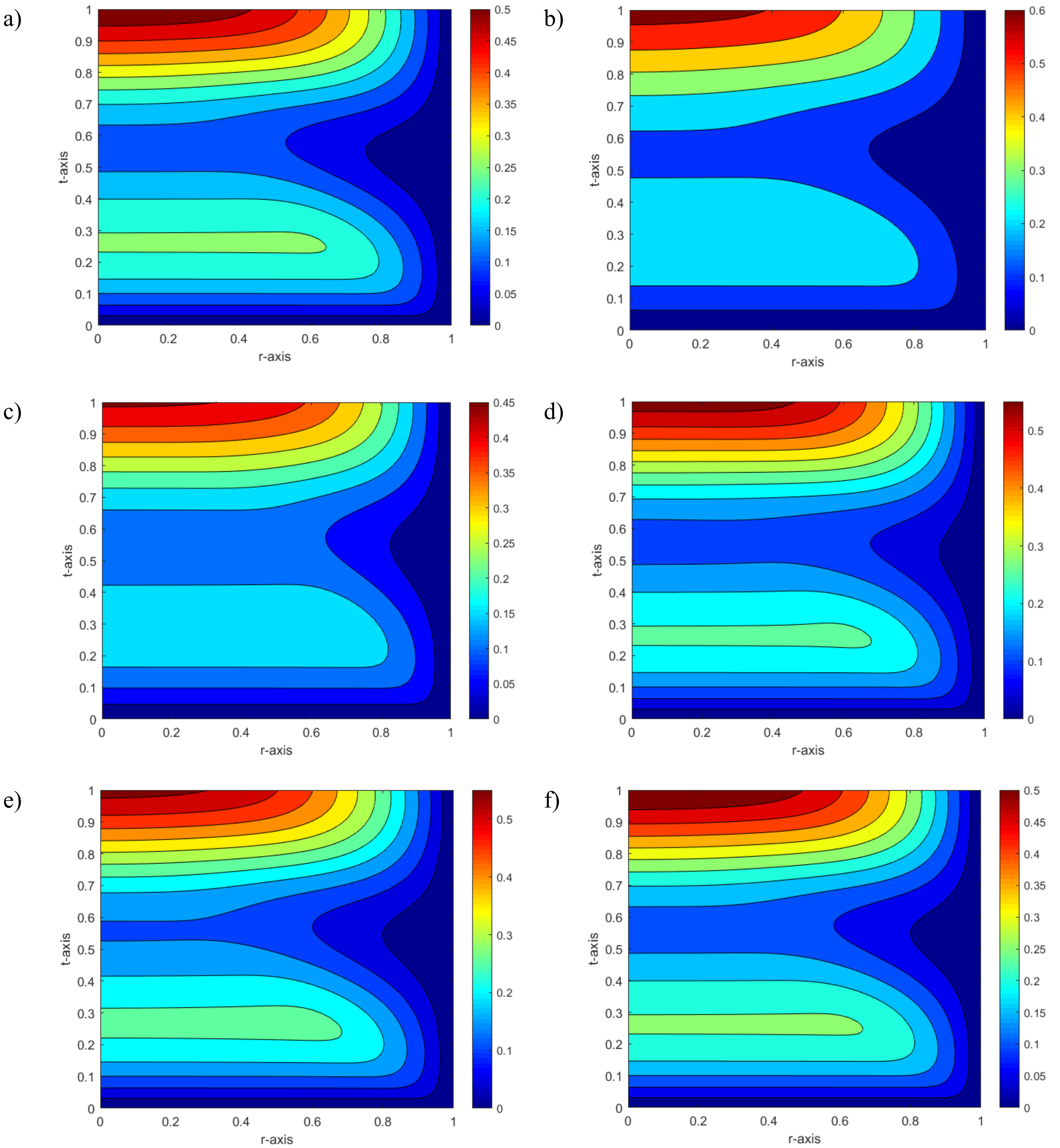

Fig.24. Velocity contour over time: (a) for default parameters, (b) without magnetic field, (c) $Re = 3$, (d) $Gr = 0.5$, (e) $Gc = 0.04$, (f) $\eta_0 = 0.3$, (g) $\Pr = 21$, (h) $A_1 = 3.14$, (i) $B_1 = 3.14$, (j) $\phi_1 = \phi_2 = 0.05$.

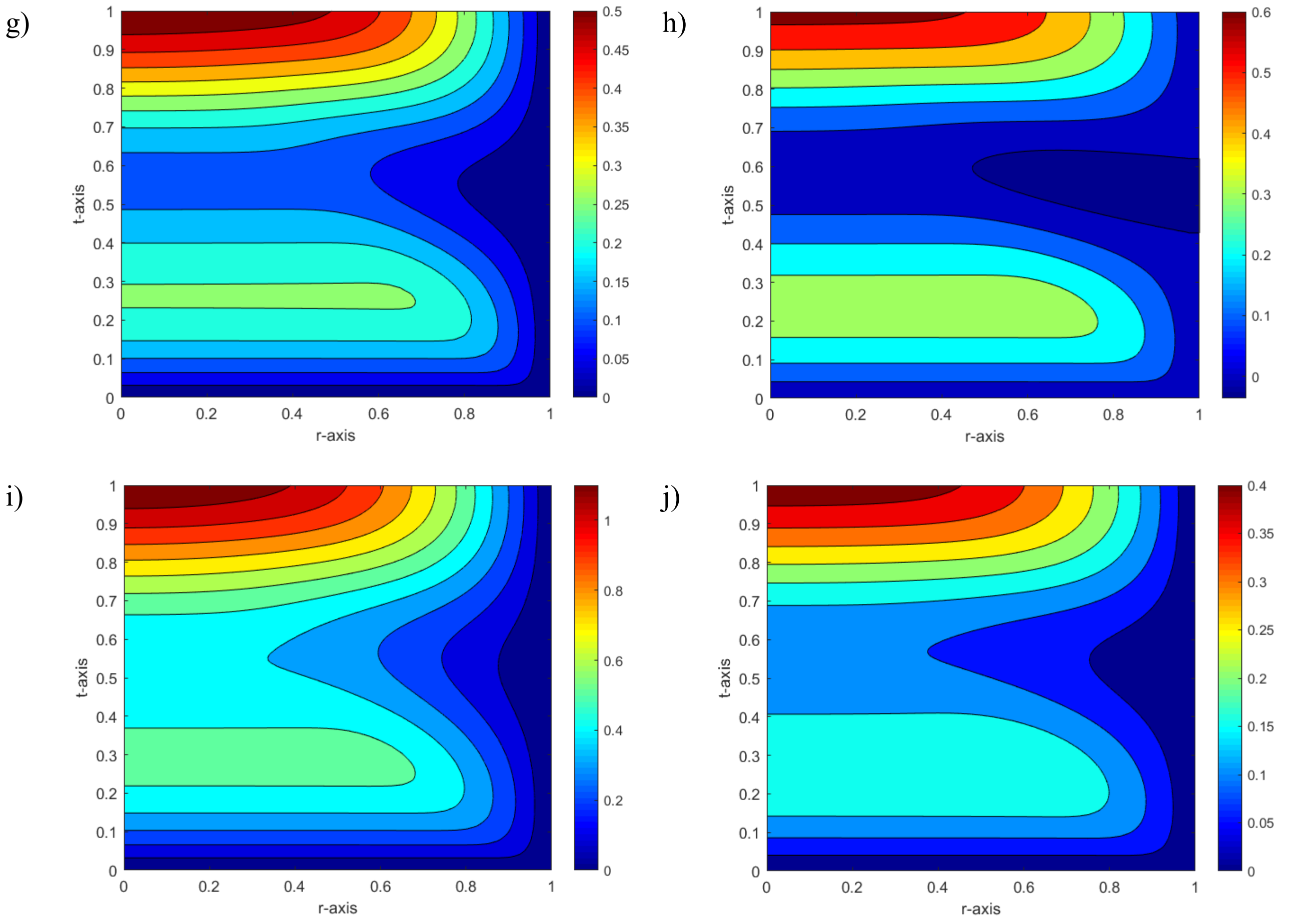

Fig.24.cont. Velocity contour over time: (a) for default parameters, (b) without magnetic field, (c) $Re=3$, (d) $Gr=0.5$, (e) $Gc=0.04$, (f) $\eta_0=0.3$, (g) $\Pr=21$, (h) $A_1=3.14$, (i) $B_1=3.14$, (j) $\phi_1=\phi_2=0.05$.

Figure 25(a) shows less concentration at the center of the artery when Reynolds changes from 2 to 3 are represented in Figures 25(a)-(b) its patterns of concentration increase.

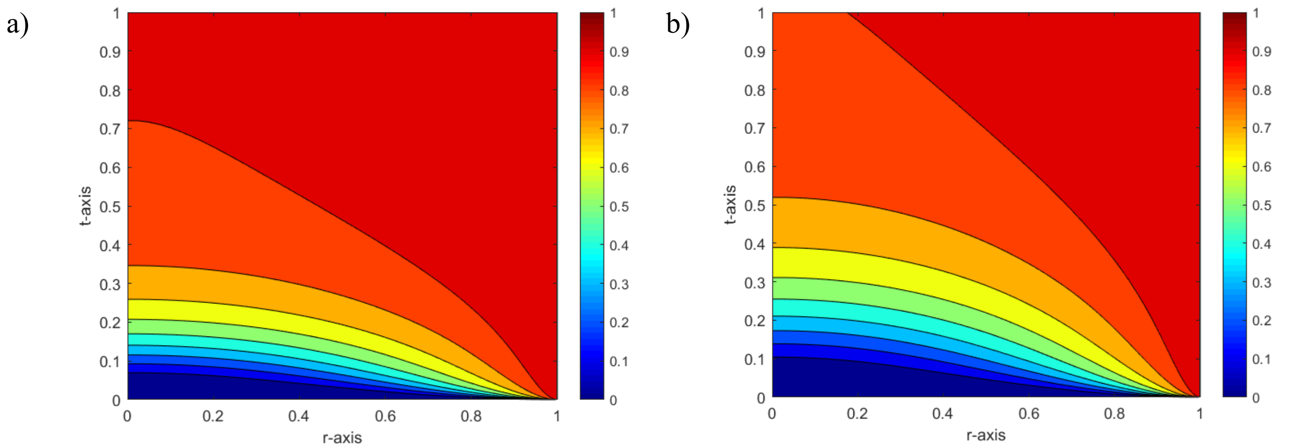

Fig.25. Concentration contour over time with: (a) $Re=2$, (b) $Re=3$, (c) $Sc=2$ and temperature contour over time with: (d) $Re=2$, (e) $Re=3$, (f) $Pr=21$.

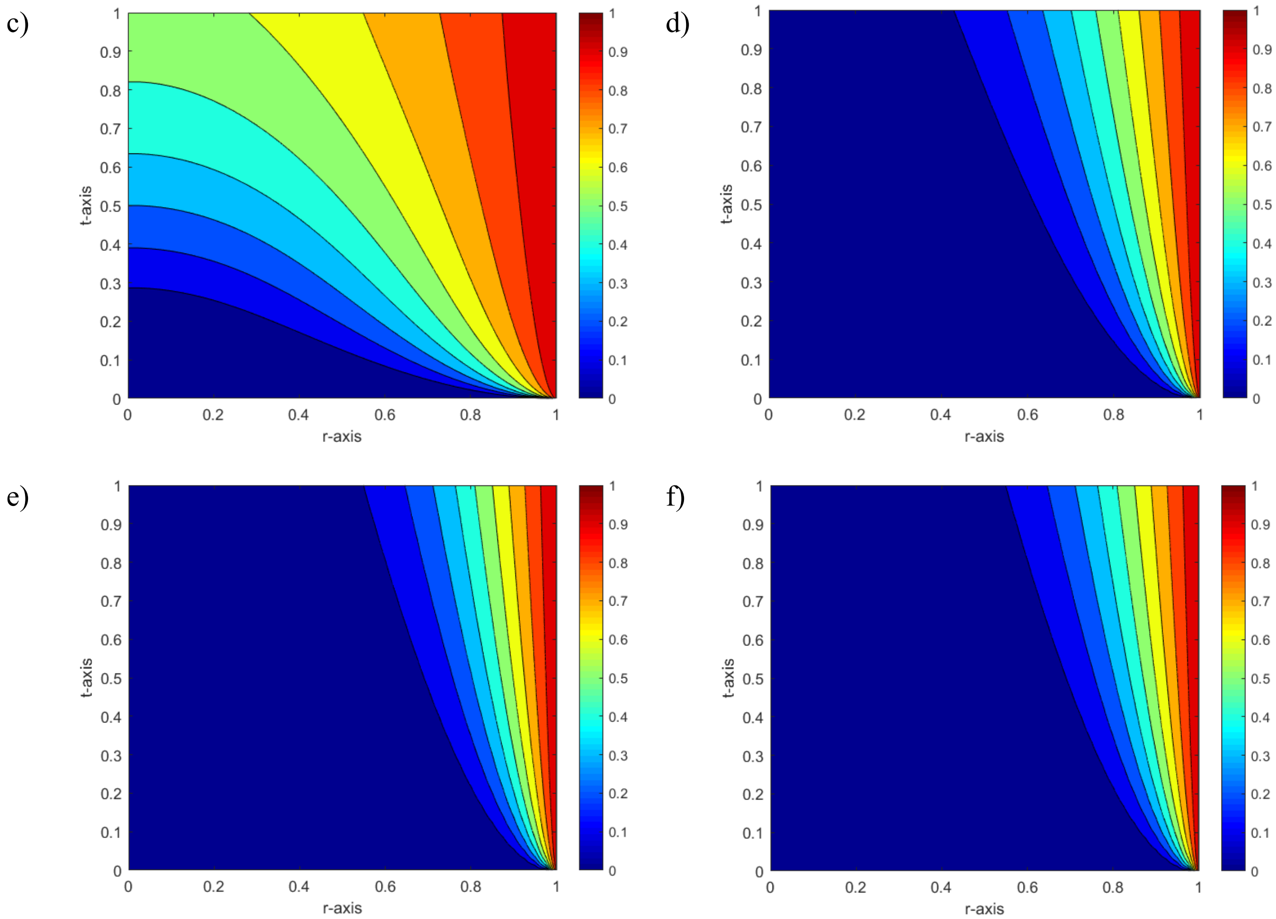

Fig.25 cont. Concentration contour over time with: (a) $Re = 2$, (b) $Re = 3$, (c) $Sc = 2$ and temperature contour over time with: (d) $Re = 2$, (e) $Re = 3$, (f) $Pr = 21$.

Figure 25(c) shows that the concentration rapidly increases when the Schmidt number is 2. Figures 25(d),(e),(f) show the temperature contour over time for different physical parameters of Reynolds number 2, 3, and Prandtl number 21, respectively. Fig.25(d) observed maximum temperature at near the arterial of the artery when Reynolds changes from 2 to 3 are represented in Figures 25(d)-(e) its patterns of temperature, not extreme changes. Figure 25(f) shows the temperature slow change when the Prandtl number is 21.

5.Conclusion

Some of the significant conclusions of the current study are listed below:

1. The velocity profiles are characterized by a pronounced enhancement with the increase of the parameters Gc, Pr and A_l which proves their direct contribution to the acceleration of the flow dynamics. Conversely, the magnetic field and Reynolds number parameters have a suppressing effect and the velocity distribution is significantly reduced.
2. When the concentration of copper nanoparticles, alumina oxide nanoparticles, and hybrid nanoparticles increases the velocity profile decreases due to the increased viscosity and momentum diffusion of the blood. It means that the stronger nanoparticles are loaded, the more flow obstacles and fluid motion inhibition are observed.

3. The temperature distributions decrease with Reynolds number, because the more intense are the convection effects, the greater are the heat transfers and the less thick are thermal boundary layers. On the same note, an increase in Prandtl number increases resistance to thermal diffusion that causes a further reduction in the temperature profile.
4. Effective thermal conductivity of copper nanoparticles, alumina oxide nanoparticles, and hybrid nanoparticles increases and consequently, their temperature profiles increase. This enhanced the ability to transport heat accelerating the absorption of energy and increasing the temperature profile of blood as a overall.
5. The concentration profiles decrease with an increase in Reynolds number because the stronger convective mixing increases the speed of mass movement and dilutes the concentration boundary layer. Similarly, increased Schmidt number decreases molecular diffusivity, further suppressing the concentration profile in the blood.
6. WSS rise when the Gr increases since forces acting on the blood that cause motion become stronger by the force of buoyancy, which acts close to the wall of the artery. Conversely, a rise in magnetic field parameter will inhibit blood velocity by the force of Lorentz resistance, thus decreasing wall shear stress.

Acknowledgment

The investigation acknowledges an improvement in the presentation due to the fruitful comments and constructive suggestions of the reviewers and editor.

Nomenclature

Gc – solutal Grashof number
Gr – thermal Grashof number
Pr – Prandtl number
Re – Reynold number
Sc – Schmidt number
u_3 – velocity
η_0 – viscosity parameter
θ – temperature
ϕ – concertation

References

[1] Kumar S. and Kumar S. (2022): *Blood flow through an elliptical stenosed artery with the heat source and chemical reaction*.– Research Journal of Biotechnology, vol.17, No.12, pp.82-90, DOI: 10.36783/rjb.v17i12.355.

[2] Kumar S. and Kumar S. (2023): *Blood flow with heat transfer through different geometries of stenotic arteries*.– Trends in Sciences, vol.20, No.11, pp.6965, DOI: 10.48048/tis.2023.6965.

[3] Ponalagusamy R. and Manchi R. (2020): *A study on two-layered (KL-Newtonian) model of blood flow in an artery with six types of mild stenoses*.– Applied Mathematics and Computation, vol.367, pp.124767, DOI: 10.1016/j.jappmathcomp.2019.124767.

[4] Sharma B.K., Kumawat C. and Vafai K. (2022): *Computational biomedical simulations of hybrid nanoparticles (Au-Al_2O_3/blood-mediated) transport in a stenosed and aneurysmal curved artery with heat and mass transfer: Hematocrit dependent viscosity approach*.– Chemical Physics Letters, vol.800, pp.139666, DOI: 10.1016/j.cplett.2022.139666.

[5] Choi S.U. and Eastman J.A. (1995): *Enhancing Thermal Conductivity of Fluids with Nanoparticles* (No. ANL/MSD/CP-84938; CONF-951135-29).– Argonne National Lab. (ANL), Argonne, IL (United States), DOI: 10.2172/166588.

[6] Algehyne E.A., Ahammad N.A., Elnair M.E., Zidan M., Alhusayni Y.Y., El-Bashir B.O., Saeed A., Alshomrani A.S. and Alzahrani F. (2023): *Entropy optimization and response surface methodology of blood hybrid nanofluid flow through composite stenosis artery with magnetized nanoparticles (Au-Ta) for drug delivery application*.– Scientific Reports, vol.13, pp.1-21, DOI: 10.1038/s41598-023-38012-7.

[7] Bacha H.B., Ullah N., Hamid A. and Shah N.A. (2024): *A comprehensive review on nanofluids: Synthesis, cutting-edge applications, and future prospects*.– International Journal of Thermofluids, vol.22, pp.100595, DOI: 10.1016/j.ijft.2024.100595.

[8] Gandhi R. and Sharma B.K. (2022): *Unsteady MHD Hybrid Nanoparticle (Au- Al_2O_3/Blood) Mediated Blood Flow Through a Vertical Irregular Stenosed Artery: Drug Delivery Applications*.– In Nonlinear Dynamics and Applications: Proceedings of the ICNDA 2022, Cham: Springer International Publishing, pp.325-337, DOI: 10.1007/978-3-030-99792-2_28.

[9] Sharma B.K., Khanduri U., Gandhi R. and Muhammad T. (2024): *Entropy generation analysis of a ternary hybrid nanofluid (Au-CuO-GO/blood) containing gyrotactic microorganisms in bifurcated artery*.– International Journal of Numerical Methods for Heat and Fluid Flow, vol.34, No.2, pp.980-1020, DOI: 10.1108/HFF-07-2023-0402.

[10] Sharma P., Sharma B.K., Mishra N.K., Almohsen B. and Bhatti M.M. (2024): *Electroosmotic microchannel flow of blood conveying copper and cupric nanoparticles: Ciliary motion experiencing entropy generation using backpropagated networks*.– ZAMM - Journal of Applied Mathematics and Mechanics / Zeitschrift für Angewandte Mathematik und Mechanik, vol.104, No.5, pp.e202300442, DOI: 10.1002/zamm.202300442.

[11] Manchi R. and Ponalagusamy R. (2021): *Modeling of pulsatile EMHD flow of Au-blood in an inclined porous tapered atherosclerotic vessel under periodic body acceleration*.– Archive of Applied Mechanics, vol.91, No.7, pp.3421-3447, DOI: 10.1007/s00419-021-01977-w.

[12] Poonam and Sharma B.K. (2022): *Mathematical Analysis of Hybrid Nanoparticles (Au- Al_2O_3) on MHD Blood Flow Through a Curved Artery with Stenosis and Aneurysm Using Hematocrit-Dependent Viscosity*.– In Nonlinear Dynamics and Applications: Proceedings of the ICNDA 2022, Cham: Springer International Publishing, pp.407-419, DOI: 10.1007/978-3-031-13123-3_37.

[13] Tripathi J., Vasu B., Bég O.A. and Gorla R.S.R. (2021): *Unsteady hybrid nanoparticle-mediated magneto-hemodynamics and heat transfer through an overlapped stenotic artery: Biomedical drug delivery simulation*.– Proceedings of the Institution of Mechanical Engineers, Part H: Journal of Engineering in Medicine, vol.235, No.10, pp.1175-1196, DOI: 10.1177/09544119211027110.

[14] Zaman A., Ali N. and Khan A.A. (2020): *Computational biomedical simulations of hybrid nanoparticles on unsteady blood hemodynamics in a stenotic artery*.– Mathematics and Computers in Simulation, vol.169, pp.117-132, DOI: 10.1016/j.matcom.2019.09.006.

[15] Ahmed B., Ashraf A. and Anwar F. (2023): *Inertial considerations in peristaltically activated MHD blood flow model in an asymmetric channel using Galerkin finite element simulation for moderate Reynolds number*.– Alexandria Engineering Journal, vol.75, pp.495-512, DOI: 10.1016/j.aej.2023.05.068.

[16] Vinita., Kumar P. and Poply V. (2023): *Mathematical modelling of magnetohydrodynamic nanofluid flow with chemically reactive species and outer velocity towards stretching cylinder*.– Journal of Nanofluids, vol.12, No.4, pp.1067-1073, DOI: 10.1166/jon.2023.1979.

[17] Makkar V., Poply V. and Sharma N. (2023): *Three dimensional modelling of magnetohydrodynamic bio-convective Casson nanofluid flow with buoyancy effects over exponential stretching sheet along with heat source and gyrotactic micro-organisms*.– Journal of Nanofluids, vol.12, No.2, pp.535-547, DOI: 10.1166/jon.2023.1932.

[18] Makkar V., Poply V., Goyal R. and Sharma N. (2021): *Numerical investigation of MHD Casson nanofluid flow towards a non linear stretching sheet in presence of double-diffusive effects along with viscous and ohmic dissipation*.– Journal of Thermal Engineering, vol.7, No.2, pp.1-17, DOI: 10.18186/thermal.882956.

[19] Manisha R. and Kumar S. (2022): *Visco-elastic fluid model in an inclined porous stenosed artery with slip effect and body acceleration*.– International Journal of Applied Mechanics and Engineering, vol.27, No.4, pp.82-104, DOI: 10.2478/ijame-2022-0052.

[20] Sharma M., Gaur R.K. and Sharma B.K. (2019): *Radiation effect on MHD blood flow through a tapered porous stenosed artery with thermal and mass diffusion*.– International Journal of Applied Mechanics and Engineering, vol.24, No.2, pp.411-423, DOI: 10.2478/ijame-2019-0026.

[21] Zaman A., Ali N. and Sajid M. (2017): *Numerical simulation of pulsatile flow of blood in a porous-saturated overlapping stenosed artery*.– Mathematics and Computers in Simulation, vol.134, pp.1-16, DOI: 10.1016/j.matcom.2016.09.008.

[22] Mishra N.K., Sharma P., Sharma B.K., Almohsen B. and Pérez L.M. (2024): *Electroosmotic MHD ternary hybrid Jeffery nanofluid flow through a ciliated vertical channel with gyrotactic microorganisms: Entropy generation optimization*.– Heliyon, vol.10, No.3, DOI: 10.1016/j.heliyon.2024.e25102.

[23] Kumar S. and Kumar S. (2025): *A study of gold nanoparticle blood flow in stenotic arteries with Arrhenius energy and variable viscosity*.– Research Journal of Biotechnology, vol.20, No.12, pp.228-240, DOI: 10.36783/rjb.v20i12.981.

[24] Zigta B. (2020): *Effect of thermal radiation and chemical reaction on MHD flow of blood in stretching permeable vessel*.– International Journal of Applied Mechanics and Engineering, vol.25, No.3, pp.198-211, DOI: 10.2478/ijame-2020-0043.

[25] Tripathi B. and Sharma B.K. (2018): *Effect of variable viscosity on MHD inclined arterial blood flow with chemical reaction*.– International Journal of Applied Mechanics and Engineering, vol.23, No.3, pp.767-785, DOI: 10.2478/ijame-2018-0042.

[26] Nandal J., Kumari S. and Rathee R. (2019): *The effect of slip velocity on unsteady peristalsis MHD blood flow through a constricted artery experiencing body acceleration*.– International Journal of Applied Mechanics and Engineering, vol.24, No.3, pp.645-659, DOI: 10.2478/ijame-2019-0040.

[27] Sudha T., Umadevi C., Dhange M., Manna S. and Misra J.C. (2021): *Effects of stenosis and dilatation on flow of blood mixed with suspended nanoparticles: A study using homotopy technique*.– International Journal of Applied Mechanics and Engineering, vol.26, No.1, pp.251-265, DOI: 10.2478/ijame-2021-0015.

[28] Kumawat C., Sharma B.K., Muhammad T. and Ali L. (2024): *Computer simulation of two phase power-law nanofluid of blood flow through a curved overlapping stenosed artery with induced magnetic field: Entropy generation optimization*.– International Journal of Numerical Methods for Heat and Fluid Flow, vol.34, No.2, pp.741-772, DOI: 10.1108/HFF-07-2023-0391.

[29] Hoffmann K.A. and Chiang S.T. (2000): *Computational Fluid Dynamics* (vol.I).– Wichita, Engineering Education System.

[30] Devi S.A. and Devi S.S.U. (2016): *Numerical investigation of hydromagnetic hybrid Cu- Al_2O_3/water nanofluid flow over a permeable stretching sheet with suction*.– International Journal of Nonlinear Sciences and Numerical Simulation, vol.17, No.5, pp.249-257, DOI: 10.1515/ijnsns-2016-0004.

[31] Gandhi R., Sharma B.K., Kumawat C. and Beg O.A. (2022): *Modeling and analysis of magnetic hybrid nanoparticle (Au- Al_2O_3/blood) based drug delivery through a bell-shaped occluded artery with joule heating, viscous dissipation and variable viscosity effects*.– Proceedings of the Institution of Mechanical Engineers, Part E: Journal of Process Mechanical Engineering, vol.236, No.5, pp.2024-2043, DOI: 10.1177/09544089221088463.

[32] Kumawat C., Sharma B.K., Al-Mdallal Q.M. and Rahimi-Gorji M. (2022): *Entropy generation for MHD two phase blood flow through a curved permeable artery having variable viscosity with heat and mass transfer*.– International Communications in Heat and Mass Transfer, vol.133, pp.105954, DOI: 10.1016/j.icheatmasstransfer.2022.105954.

[33] Sharma B.K. and Kumawat C. (2021): *Impact of temperature dependent viscosity and thermal conductivity on MHD blood flow through a stretching surface with ohmic effect and chemical reaction*.– Nonlinear Engineering, vol.10, No.1, pp.255-271, DOI: 10.1515/nleng-2021-0020.

[34] Sharma B.K., Gandhi R. and Bhatti M.M. (2022): *Entropy analysis of thermally radiating MHD slip flow of hybrid nanoparticles (Au- Al_2O_3/Blood) through a tapered multi-stenosed artery*.– Chemical Physics Letters, vol.790, pp.139348, DOI: 10.1016/j.cplett.2022.139348.

[35] Tanveer A., Ashraf M.B. and Masood M. (2024): *Entropy analysis of peristaltic flow over curved channel under the impact of MHD and convective conditions*.– Numerical Heat Transfer, Part B: Fundamentals, vol.85, No.1, pp.45-57, DOI: 10.1080/10407790.2023.2205510.

Received: September16, 2025
Revised: June 12, 2026